Proceedings of the Institution of Mechanical Engineers, Part C: Journal of Mechanical Engineering Science,
Vol. 232, Issue 10, 2018, pp. 1898-1924
DOI:10.1177/0954406217707984

Heat dissipation from a stationary brake disc

Part 2: CFD Modelling and Experimental Validations

Marko Tirovic and Kevin Stevens, Cranfield University, Cranfield, MK43 0AL, UK

Abstract

Following from the analytical modelling presented in Part 1, this Paper details a comprehensive Computational Fluid Dynamics (CFD) modelling of the 3-dimensional flow field around, and heat dissipation from, a stationary brake disc. Four commonly used turbulence models were compared and the Shear Stress Turbulence model was found to be most suitable for these studies.

Inferior cooling of the anti-coning disc type is well known but the core cause in static conditions was only now established. The air flow exiting the lower vane channels at the inner rotor diameter changes direction and flows axially over the hat region. This axial flow acts as a blocker to the higher vane inlets, drastically reducing convective cooling from the upper half of the disc. The complexity of disc stationary cooling is further caused by the change of flow patterns during disc cooling. The above axial flow effects slowly vanish as the disc temperatures reduce. Consequently, convective heat transfer coefficients are affected by both, the change in the flow pattern and decrease in air velocities due to reduced air buoyancy as the disc cools down.

As in Part 1, the special Thermal Rig was used to validate the CFD results quantitatively and qualitatively. The former used numerous thermocouples positioned strategically around the brake disc, with the latter introducing the concept of laser generated light plane combined with a smoke generator to enable flow visualisation. Predicted average heat transfer coefficients using CFD correlate well with the experimental values, and even 2D analytical values (as presented in Part 1) reasonably closely follow the trends. The results present an important step in establishing cooling characteristics related to the Electric Parking Brake application in commercial vehicles, with future publications detailing heat transfer from the entire brake assembly.

Keywords: Stationary Disc; Brake Disc; Computational Fluid Dynamics; Heat Dissipation; Convective Cooling.

Nomenclature:

Symbol	Description
A	Surface area
C_p	Specific heat capacity
D	Diameter
E	Energy
$\bar{f}$	Single representation for other forces
h	Bulk heat transfer coefficient
l	Length
L	Characteristic length
m	Mass
p	Pressure
Q	Power
r	Radius
Re	Reynolds number
t	Time
T	Temperature
ρ	Density
σ	Stefan-Boltzmann constant (5.67037 E-8 $Wm^{-2}K^{-4}$)
σ_{sd}	Standard deviation
τ	Stress tensor
$\bar{v}$	Flow velocity vector

Subscripts

avg	Average
$cond$	Conduction/Conductive

$conv$	Convection/Convective
d	Disc
i	Inner
int	Interface
o	Outer
rad	Radiation/Radiative
surf	Surface
total	Total
w	Wall
∞	Ambient

Abbreviations

CFD	Computational Fluid Dynamics
CV	Commercial Vehicle
CFD	Computational Fluid Dynamics
EPB	Electric Parking Brake
FE	Finite Element (Method)
HTC	Heat Transfer Coefficient
ID	Inner Diameter
OD	Outer Diameter

1. Introduction

This paper, following from Part 1, details Computational Fluid Dynamics (CFD) modelling of the flow and heat transfer from a stationary commercial vehicle brake disc in still air. Figure 1 shows the disc CAD model and CFD modelling space for the brake disc used throughout this research, as detailed already in Part 1 of the Paper.

This paper investigated the generic disc only scenario, as shown in Figure 1, with the caliper and pads to be added later. In all analyses the disc was assumed to be heated uniformly to an elevated temperature, then kept stationary and cooled down in still air. The measurements and analyses were simultaneously conducted throughout the research but for clarity the presentation was split in two parts: Part 1 dealt with analytical derivation of convective heat transfer coefficients for disc surfaces. These were used to predict disc temperatures during the entire 6 hour cooling period, which required development of a numerical solution (using MatLab). The results were compared with measurements conducted on a specially developed Thermal Rig. Good correlation was achieved for most complex modelling case, which concluded that a change of convective and radiative heat transfer with temperature throughout the cooling period is required for accuracy when predicting temperatures during stationary parking applications. Experimental investigation was presented in detail, including the Thermal Rig equipment, test procedure, measurement and instrumentation systems. Detailed uncertainty related to temperature measurements was also documented. Emissivity of disc surface was also established.

In Part 2, CFD analyses of the disc will be conducted, predicting the flow patterns, air velocities, air temperatures, and local and average convective heat transfer coefficients. The results were validated through experiments, conducted on the same Thermal Rig and using the same equipment as in Part 1. A qualitative and quantitative experimental validation procedure was developed to confirm the predicted flow patterns, air temperatures and heat transfer coefficients.

2. CFD Modelling – Model Constriction

This section aims to progress the knowledge previously acquired by focusing on the 3-dimensional flow field generated around a stationary ventilated brake disc subjected to natural convection. The standard CFD modelling approach to such problems was utilised (Ansys CFX Code), with airflow velocities, air temperatures and convective heat transfer coefficient (h_{conv}) distribution results acquired.

CFD has been developed and used for many years now, becoming common practice when conducting airflow analysis. The greatest asset of CFD for this study is the ability to produce flow predictions within brake disc channels, where it would be otherwise impossible to see the effects of geometry on temperature and airflow patterns. From the literature, it appears Olphe-Galliard [1] is the only author who has attempted to use a generalised CFD program to predict airflow around a stationary passenger car disc brake. A discussion on the CFD model generation process is presented before the results of a test into the relative effectiveness of four generalised CFD turbulence solutions are examined.

2.1. Volume Mesh Generation

Initial modelling of airflow around a complex shape, such as a ventilated brake disc, driven purely by buoyant affects has proven difficult. Olphe-Galliard [1] found that a much larger volume has to be considered, compared to the axisymmetric models often used in dynamic braking simulations, such as Voller [2] and Galindo-Lopez [3]. Furthermore, a much finer volume mesh was required, including prism layers close to the surface boundaries, giving greater near-wall shear stress evaluation. Building on the previous work, Figure 1b shows the rectangular geometry encased around a standard 434/234 mm radial vane commercial vehicle (CV) brake disc, making the CFD volume mesh. The geometry extended 1.0 m downwards in the negative Y direction and in both the positive and negative X direction from the origin (located on the flange face plane, on the disc centreline), 0.5 m from both the flange and the inboard contact faces (Z directions), whilst extending a further 2.5 m above the disc brake (positive Y). The consequence of such a large area is that the CFD solver had to make calculations for a total volume of 3.795 m^3. Having to use a relatively fine mesh over such a large volume will inherently cause long computational time.

The mesh used for the duration of the CFD investigation is presented Figure 2; a cut through the centre of the YZ plane is shown for all three sections. Figure 2a) displays the full volume mesh that was created by a total of 9.2 million elements. Of these, 6.3 million were tetrahedral, 2.8 were wedges and the final 0.1 million were the near-wall prism elements. As seen in Figure 2b) the mesh density gets finer towards the brake disc surface boundary, with a part of the prism mesh displayed in Figure 2c. Olphe-Galliard [1] conducted a grid convergence study to show the mesh quality generated was adequate; this investigation used the same meshing strategy and therefore also generated an adequate mesh quality.

The prism layer itself was extended around the entire disc boundary surface. There are two methods of creating a prism (or inflation) layer, the first is to set the thickness of the first layer only and the other is to set the total thickness of the prism layer. With the former, there is a smooth transition between the prism layer and the tetrahedral elements and has superior capabilities when meshing with complex geometries, but does have the disadvantage that the number of layers used does vary. Alternatively, the constant layer thickness option keeps the same total thickness of the inflation layer around the surfaces but can change the number of prisms in the layer. To understand why this might be an issue, the y^+ term is discussed.

Near wall interactions are always important; however often in turbulent flow the near wall interaction is less important than the free stream flow because of the small boundary layer. In these cases, the first element away from the wall is treated as the laminar near wall region with the remaining elements in the turbulent region. Special near wall functions are built into CFD programs to deal with these laminar regions differently than in the turbulent regions. To calculate the distance, the first node needs to be away from the wall, Δy, the follow equation is used.

$$\Delta y = Ly^+ \sqrt{\left(74 {Re_L}^{-13/14}\right)} \quad (1)$$

Where L is the flow characteristic length scale, Re_L is the Reynolds Number based on the flows characteristic length and y^+ is the desired value. Using equation (1), taken from Release Notes for FLUENT 6.3 [4], the thickness of the first prism layer can be determined by using a desired value of y^+, which is a non-dimensional distance. High values, above 100, are for turbulent flow, and can be

into the thousands for high speed aerofoils. A high value of y^+ describes laminar flow is present throughout the first wall element, with no laminar flow in the following element. Having a too high a y^+ value will result in the first element being placed too far outside the boundary layer and subsequently using laminar wall functions on regions of turbulent flow. Conversely, by using a value that is too small a value under predicts the size of the boundary layer, introducing errors into the simulation; values smaller than 11 are generally deemed as too low (Jerhamre and Bergstrom [5]).

However, wall functions are only important when the flow regime is turbulent. In Part 1 it was concluded that the flow regime will be in a transitional phase over the disc brake. This lower velocity flow driven under natural convection, will require a small y^+ value to capture the more significant shear stress factors associated with natural convection flow all the way through the boundary layer, resulting in y^+ values below 11 are likely to be needed. Standard wall functions therefore cannot be used. Scalable wall functions allow the flow to be resolved all the way through the boundary with a finer near wall (prism layer) mesh and consequently, one was used throughout this investigation.

With the flow not expected to be fully turbulent, a smaller first layer thickness of 0.075 mm was used with an exponential growth rate to ensure the laminar effects were captured; this relates to an estimated y^+ value of 5. A maximum of 10 layers was set but as the first layer thickness prism layer meshing scheme was used, this number can be smaller in complex geometry regions. The advantage of a smooth transition from the prism layer and the tetrahedral elements was one reason for using first layer thickness meshing scheme, but it was the guaranteed smaller size of first layer thickness which was the main factor behind the scheme application. The software used to produce this mesh was ANSYS Mesh version 12.1 solver.

2.2. CFD Model Setup

With a completed mesh, attention turned to setting up the CFD model. Parameters that needed defining were the open surfaces temperatures, disc brake surface temperatures, which turbulence model would be used in the solver and what was the desired convergence target. Starting with the temperatures, the open type boundary surfaces (displayed in Figure 1b) were set to an ambient 20°C. As the disc was

heated to 400°C initial temptation was to match the disc brake surface boundaries with temperatures. However, as the disc brake had to rotate during heating, air temperature measurements were recorded after the disc brake friction surfaces had been allowed to cool to 350°C, ensuring no rotational effects remained from the heating process. All resultant airflow was then a function of natural convection. CFD surface temperatures were therefore set at 350°C on the rotor. Conduction to the hat section of the disc brake would cause its temperature to rise, but dissipation by radiation and convection will result in the temperature being less than the friction surfaces; the hat was assumed to be at 200°C (detailed description of disc surfaces was given in Part 1 of the paper).

Convergence levels from a CFD model is determined by the size of the residual values produced from the solver compared to a predetermined target value. A model is said to be complete once all the governing equations have reduced to the specified value. The residual values are a resultant of the truncation error generated in the solver, when truncating the numerical approximation series equations. Convergence analysis has been covered in-depth by Galindo-Lopez [3] and was found that to achieve good agreement between CFD and experimental results, for both momentum and heat transfer, a convergence target of $1e^{-5}$ should be used, which was subsequently selected and used in this investigation.

Selecting the turbulence model was somewhat less straightforward. The amount of work readily available in the literature on natural convection airflow around a stationary disc brake is minimal. Subsequently, there is limited advice as to which turbulence method is best suited. Numerous authors have published work using the $k-\varepsilon$ model in dynamic scenarios because of its robustness and quick convergence times associated with it, whilst $k-\omega$ models have been used for wall-bounded flows. As Figures 1b and 2 show, the volume is partially wall bounded (in the vane channels) and partly free stream so either of these turbulence models could be used. Also, with the flow regime possibly transitional, a simple laminar model may well prove to the most appropriate to use.

In response to the lack of published work, CFD predictions were generated with four separate models. Each simulation used a different turbulence, with the purpose of determining which turbulence model

is most appropriate to apply when modelling stationary disc cooling. A short discussion is offered first about the three mentioned turbulence models, as well as a fourth (being the Shear Stress Transport (SST) model), before the results are presented.

2.2.1. Laminar Model

In CFD generalised codes, the fundamental equations that are being calculated are the unsteady Navier-Stokes equations, in the general form:

$$\rho\left(\frac{\partial \bar{v}}{\partial t} + \bar{v} \cdot \nabla \bar{v}\right) = -\nabla p + \nabla \cdot \tau + \bar{f} \tag{2}$$

Where $\bar{v}$ is the flow velocity vector, τ is the stress tensor and $\bar{f}$ is a single representation for other forces that may be acting in the system. For simple laminar flow, the Navier-Stokes equation breaks down into the continuity equation and the conservation of momentum. The former calculates properties related to the mass within the system whilst the latter calculates the 3-dimensional flow properties. This process requires four equations to be solved for each node. If heat transfer is present in the simulation, a conservation of energy is also calculated. In this case, diffusion is the mechanism for energy transfer within the fluid. The laminar model can be used for high Reynolds Number flow but with additional terms are required as there are no mathematical terms to deal with the added energy components.

2.2.2. $k - \varepsilon$ Model

The $k - \varepsilon$ turbulence model is by far the most common model used when conducting CFD analysis. To aid the governing Navier-Stokes equations with the presence of flow turbulence, the $k - \varepsilon$ model calculates two additional equations, or transport equations, at every element. The first is to calculate k, the amount of turbulence kinetic energy. The second ε equation is for the turbulence eddy dissipation rate. One disadvantage of this model is that it was derived for purely turbulent flow so will produce inaccurate results if used for any other flow regime. Robustness is achieved when using the two additional equations that generate reasonable accuracy (provided in turbulent conditions), for economical computation times. These factors are the source behind why it is commonly used throughout research and industry.

2.2.3. $k-\omega$ Model

Like with the $k-\varepsilon$, the $k-\omega$ turbulence model uses two transport equations to calculate the additional turbulent energy; the turbulent kinetic energy, k, equation remains with the specific dissipation rate, ω, replacing the turbulence eddy dissipation rate. Terms in the ω equation allow molecular viscosity effects to be calculated, giving the desirable characteristic of accurately calculating near-wall boundary layer flow.

However, the main problem with the standard $k-\omega$ model is that it is extremely sensitive to free stream flow. The baseline (BSL) model is a slight derivation of the original $k-\omega$, it was established to give the robust and accurate near-wall region flow predicts generated by the $k-\omega$ but with the advantage of also delivering the free-stream properties of the $k-\varepsilon$ model. To do this, the $k-\varepsilon$ equations are transformed and added to the $k-\omega$ equations. By implementing a blending function, the BSL model differentiates between the two sets of equations with respect to each element relative position. In near-wall regions, the blending function is one and zero in the free stream, the reverse is true for elements in the free stream region. Consequently, $k-\omega$ based models are widely used for simulations where the flow is constrained by walls.

2.2.4. SST Model

The SST turbulence model theoretically improves on the BSL models as it introduces terms to the transport equations that calculate the transportation of turbulent shear stress. The omission of turbulent shear stress in the BSL model prevents accurate predictions of flow separation under pressure gradients and/or from smooth surfaces (Menter [6]).

2.2.5. Turbulence Modelling Comparison

To test the validity of the four discussed turbulence models, temperatures were recorded during the practical experiment from the thermocouples and will be compared to the four CFD models. Table 1 shows the amount of time each model took to reach convergence. Having to calculate the fewest number of equations per iteration, it was unsurprising that the laminar model was the quickest to complete. It

transpired that the SST turbulence model is the quickest out of the remaining three to converge for a disc CFD simulation. The effects of having turbulent shear stress terms in the SST model greatly improve the time to convergence when compared to the other $k-\omega$ derivative as the BSL model took virtually double the amount of time, whereas the $k-\varepsilon$ model was approximately 11.5 hours longer than the SST.

Table 1: CFD model tests – convergence times

Turbulence Model	Time to convergence [days h:min:s]
Laminar	2 04:58:04
$k-\varepsilon$	2 21:24:02
BSL	4 05:39:36
SST	2 09:57:15

It should be noted here that none of the models fully converged to the $1e^{-5}$ limit set. Instead, this time was until the limit of 1,750 iterations was reached. In all cases, the mass and three momentum equations did indeed reach the residual limit in the allowable region (Figure 3a), what prevented full convergence was the heat transfer properties (Figure 3b). The residual values in each of the models quickly reduced to $1e^{-3}$ before plateauing and remaining constant for the remaining calculations. Clearly, limitations of the current solver capabilities for such a complex problem were reached. However, considering all the momentum equations successfully converged with the heat transfer residuals all converging to a similar satisfactory level, albeit not to the desired level, the results could still be acceptable if the predicted temperatures were close to the measured. More details on modelling and other aspects presented in this Paper are given by Sevens [7].

Thus far, the only analysis conducted has been on the speed of convergence. In section 7.2, the predicted air temperatures using the various turbulence models are compared to experimental data. It is shown that the SST models is most appropriate to use for stationary disc simulations, due to its combination of speed and accuracy. Therefore, all further results presented in this paper were generated using the

SST turbulence model. Having defined the CFD setup procedure, results of the CFD simulation will be presented in three subsections and discussed individually; air velocities, air temperatures and coefficients of convective heat dissipation.

3. CFD Results – Air Velocities

An advantage of CFD utilised for this investigation is that the same CFD model, including the mesh, used previously could be deployed once again by modifying the disc brake surface temperatures. In addition to the initial temperature modelled (350ºC for the rotor and 200ºC for the hat area of the disc), three further friction surface temperatures were used, based on the bulk rotor temperature found experimentally, which were 213°C, 112°C and 49°C. Corresponding hat temperatures were 175°C, 112°C and 49°C respectively. Noticeable changes in the airflow patterns and the distribution of convective dissipation have been discovered.

CFD analyses enable numerous results to be generated. Most attention was spent processing and showing air velocities and heat transfer coefficients, with air temperature and static pressure giving further insight and building confidence in the flow patterns predicted. This was done for regions of particular interest; the disc (rotor) friction surfaces, mid-plane of the vane channel, the axial plane and the hat surface.

Due to the inability to assume rotational symmetry about the vanes, the results presented here correspond to the convention shown Figure 4. The vertical centreline was taken from the top vane, centre vane channel (position 0°), when looking at the outboard friction surface. Positive angles represent a clockwise position from the vertical centreline, whist negative values are anti-clockwise position.

3.1. Air velocities at the start of cooling period

The flow results will be first presented in the plane located at the centre of the vanes (mid disc rotor thickness), parallel to the friction surfaces. Figures 5 and 6 show the velocity streamlines originating in this plane. It is clear that only a limited amount of air that started on the plane remains there, or even

remains close to the plane of origin. Deflection of the air streams happens in two forms, the first being the influence of the outer brake disc surfaces. Accelerating air below the disc brake rises vertically and is forced to deflect when it comes into contact with the relatively bluff circumferential surface. Considerably more air is deflected around the outside of the disc brake than what enters the lower vanes (90° to 180°). Air exiting from these lower vanes, at the ID, accumulates some axial momentum in addition to the vertical momentum, due to the disc brake geometry, providing the second source of airflow deflection. Exiting airflow subsequently travels over the hat section, producing the highest predicted air speeds in the domain, with values reaching 1.7 m/s.

For analytical calculation purposes (see Part 1 of the Paper), buoyant airflow over a disc brake surfaces has historically been considered as two-dimensional. Using this assumption enables the friction surfaces of the walls to be treated as flat plates, allowing dimensionless analysis of Rayleigh and Nusselt numbers to provide an end convective heat transfer coefficient value. Coupling 2D flow with the ideal gas laws suggests that as the air gains thermal energy, the density drops and rises over the surfaces and through the vanes. CFD results in the form of streamlines present evidence in both Figures 5 and 6 that only a small volume of air enters or exits the vanes at the OD, in the region between 45° and 135° from the vertical centreline, when compared to the amount exiting at the ID from the lower vanes.

As the highest air speeds are not seen at the highest point on the disc brake, a more sophisticated approach than the simplified 2D approach to disc brake cooling must be adopted. Subsequently, the traditional methods can be used successfully to predict basic flow properties of a solid disc, but not to accurately predict the highly complex 3D airflow patterns for stationary, ventilated disc brake applications.

Figure 6 divulges a little more information to what was shown in Figure 5, as the walls of the disc brake have been removed, allowing visual access to the in-vane flow. The in-channel velocities are lower than on the outer disc surfaces, with the maximum channel speed being only 0.8 m/s. As flow recirculation is a function of low flow energy, the rate of thermal energy transfer to kinetic energy from the channel walls to the flowing air must be low for the occurrence of these recirculation regions to develop. These

interesting findings will be explored later, when looking at air temperature and static pressure distributions.

Remarkably, dual recirculation is present in the vane channel located 36° from the vertical centreline, as blockages prevent air from entering or exiting the vane at either the OD or ID (see Figure 6). Convective cooling in these channels is negligible with almost no airflow transpiring through it. External flow is the greatest cause for this, as the angle that the air has to deflect from the free stream and into the vane channel OD is now too great. External airflow has been shown to cause dual recirculation regions before [8] but only when the wheel is attached during rotational simulations. A simplified scenario is simulated here with no caliper components or a wheel, which are likely to further hinder the channel airflow, suggesting the anti-coning disc brake design may cool even worse than what was depicted.

It is also interesting to monitor air flow around the hat section (disc hub). Figure 7a shows streamline velocities for the lower section of the hat in ZY plane, at 200°C (with corresponding rotor temperature at 350°C). Starting on the lower portion of the disc brake, it can be seen that accelerated air within the vane turns 90° on exit and flows axially along the hat section. This exiting axial airflow entrains the air on the outside of the vanes, taking the main stream away from the ID. It is the effect of this entrainment process that prevents the airflow from entering the upper vanes ID, creating the entrance blockage. An apparent flow characteristic that is also shown in Figure 7b is the propagation of an external recirculation region. The cause of this region is the axially moving air coming into contact with the bluff surface of the bolt fixing section (disc flange). The kinetic energy after impact with the surface is not sufficient to re-join the main stream, resulting in the flow folding back in on itself.

3.2. Change of Air Flow during cooling

3.2.1. Brake disc

Figure 8 shows streamlines from the vanes mid-plane (XY) for rotor at 112ºC, with the corresponding hat temperature of also 112ºC. When compared to Figure 5 (rotor at 350ºC), there are considerable differences, not only in lower air velocities (which is expected) but also to air flow pattern. It is clear

that air flowing around the hat section has little to no axial momentum. This is true until the air approaches the top of the hat (the 0° position), where it is drawn from the bolt section back across the hat and into the vanes. The pull from the in-channel low pressure is now stronger than the external flow entrainment.

3.2.2. Hat

Airflow around the hat is shown again in the ZY plane, for the lower (a) and upper (b) portions in Figure 9. The hat is at 175°C (with corresponding rotor temperatures at 213ºC). In comparison with Figure 7a, for the hat at 200°C, the stagnation point is still present on the outboard friction surface. Originally, low energy air near the stagnation point at the 0° position, on the outboard friction surface, was pulled down with a proportion going into the channel. At a lower friction surface temperature, the axial velocity is lower, enabling virtually all the air on the outboard surface to join the free-stream. Subsequently, there is a reduction in air flowing through the central, upper vane channels, which will reduce local in-vane convective heat transfer.

Figure 9 demonstrates air flowing around the hat section has little to no axial momentum. This is true until the air approaches the top of the hat (the 0° position), where it is drawn from the bolt section back across the hat and into the vanes. The pull from the in-channel low pressure is now stronger than the external flow entrainment.

Finally, airflow characteristics for the lowest friction surface temperature simulation (49°C) will be examined. Figure 10 shows streamline velocities for the hat in ZY plane, at 49°C (with corresponding rotor temperature at 49°C). Starting in the axial plane once again, Figure 10 shows a significant change to previous airflow patterns. The recirculation at the bolt fixing section has now completely disappeared, with a new recirculation appearing at the ID, in the vane channel exit. This has a hugely contrasting effect to previous temperatures because the external free-stream flow now has a higher amount of energy than the exiting airflow from the vane channel. In fact, instead of the airflow having axial momentum away from the outboard friction surface, the reverse is seen with air flowing inwards, towards the rotor ID, although the predominant motion is vertically upwards.

4. CFD Results – Air Temperature and Static Pressure

4.1. Air Temperature Distribution

Figure 5 and Figure 6 showed that air replenishment is not happening in large channel areas. The air exiting ventilation channels at the lower half of the disc (towards disc ID, directed outboard) is flowing upwards and preventing fresh air entry into the upper channels. This is expected to cause and increase in air temperatures in these, upper channels. Indeed, as shown in Figure 11 the air temperatures in the vanes are high, reaching a maximum of 623 K or equalling the rotor temperature (350°C). Figure 11 is showing air temperatures in the mid-plane (XY) but there is little difference within the cross section of channels in axial direction. Most air is entering the channels at the bottom of the disc (from OD, see Figures 5 and 6), where air temperatures are the lowest (Figure 11).

The disadvantageous effect of recirculating low density air at the channel ID is that these regions act as barriers for the free air entering the channels. A detrimental cycle arises where recirculating air is formed due to the low energy air flow, but the low density recirculation blocks higher energy flow from entering the vane. Consequently, the cooling performance of this (anti-coning) type ventilated disc under stationary conditions is severely compromised.

4.2. Static Pressure Distribution

Static air pressure distribution (in the same XY mid-plane, using SST model), shown in Figure 12 further illustrates why the exiting lower ID airflow had a greater amount of molecules passing through a smaller area. Heat energy transferred to the air via convection causes the air to increase in temperature. As it does it expands, reducing in density. However, the lower vane channels are shaped like a converging duct, causing a greater amount of air molecules to pass through a smaller cross-sectional area, which increases the in-channel pressure and ultimately the air velocity. Low pressure air external to the vanes is consequently not able to enter the vanes in this location, causing the blockage effect previously discussed.

5. CFD Results – Distribution of Heat Transfer Coefficients

This anti-coning disc geometry, when rotating, also shows inferior cooling characteristics to the standard design. Instead of air entering straight into the channels in the standard design, here the air from the hub surface (disc ID) must turn 90° before air entering the channels. This is the main reason for poorer cooling characteristics when compared to the standard disc design, as this directional change reduces the volume and speed of the air entering the channels, when the disc is rotating. However, this is only partly the main reason for poor static cooling performance.

So far, the distribution of air velocities, air temperature and static pressure showed very consistent and logical results, pointing out on the other important reasons for lower heat dissipation of this, anti-coning type of the disc in static conditions. The effects were not previously known or understood but it is obvious that the air exiting the channels from the lower half of the disc is actively preventing replenishment of the air in the upper half of the channels.

Presented here is the first attempt at understanding the distribution of the convective heat transfer coefficients, h_{conv} values in stationary conditions. The results are split into two sections, the first being the generated convective heat transfer coefficients at highest temperature (start of cooling, rotor at 350°C), with further results investigating the change in h_{conv} values as disc cools down, i.e. temperatures drop.

5.1. Convective heat transfer coefficients at the start of the cooling

Looking now at external surface heat dissipation, Figure 13 shows that there is only a small variation in h_{conv} values between the upper and lower sections of the outboard friction surface. Values generally remain close to 11 W/m^{2}K throughout the entire surface, increasing only slightly towards the OD. A sharp increase is evident directly at the OD, with exceptionally high values greater than 30 W/m^{2}K displayed. The model was simplified at the disc brake edges by removing the chamfers and a finer mesh was not used in this region either. These actions were necessary to prevent the computational time from extending further, thus the high local values produced in Figure 13 (and Figure 14) can be attributed to

these actions, resulting in inaccurate predictions. Still, the influence is only minor since the areas of high h_{conv} values are very small (<2%) in comparison with the entire disc wetted area. Indeed, high heat transfer coefficient values is a characteristic of the start of a boundary layer, however these extreme values are present on both the beginning and ending regions of the flow and are an order of magnitude larger than the average across the friction surface. For these reasons, it was correct to consider these values as erroneous. Since the total area where the error occurs is less than 2% of the total surface area, their influence on the global cooling pattern is minimal.

There is an omission to the generalisation made of a relatively constant outboard h_{conv} value, and that is in the 0° vicinity (see Figure 4 for angular convention). The stagnation point on the outboard friction surface, discussed previously, is the cause of this h_{conv} drop-off. The absence of air movement inhibits the convection process from occurring, hence the predicted low coefficient value. Interestingly, the same distribution pattern is seen on the inboard friction surface, but with a reduced area of low h_{conv} values. Being of an anti-coning configuration, the suction from the low in-channel air pressure cannot be the cause of the reduced h_{conv} region like on the outboard surface. Instead, it is a simple function of geometry. Vertically travelling air comes into contact with the bluff ID surface, forcing it to dramatically change direction rather than having a smooth transition to the friction surface; the latter would eliminate the area of low convection.

By removing the disc brake (rotor) faces, Figure 14 shows the variability in convective dissipation within and from the channels. Wall effects aside, the largest values are seen on the lower channel walls, reaching 5 W/m^{2}K. Reasonable values are maintained for the middle section (45° to 135°), except in the regions of recirculation, where heat transfer is reduced. Low heat transfer is also seen for in the vanes between 0° and 45°, attaining only 3 W/m^{2}K at the OD. For the dual recirculating channel at 36°, the heat transfer via convection is negligible, as predicted by the velocity streamline results.

To complete the heat transfer coefficient (HTC) distribution study, h_{conv} values over the hat section are discussed. Setting the surface temperature across the hat section to a constant 200°C should result in reduced h_{conv} values when compared with the disc brake friction surfaces. Indeed, this is the case

for the most part, shown in Figure 15 values are around 3 W/m^{2}K. There is a sharp rise in h_{conv} towards the 0° circumferential position. Air flowing around the hat section, with a Re value approximately 19,000, detaches prior to this point to create a low pressure region. Air is resultantly pulled down off the outboard surface, forming the stagnation point displayed in Figure 7b. This sucking effect increases the axial velocity component in the air, increasing the local h_{conv} value. With the largest thermal gradient present between the friction surfaces and air, rather than between the hat and air, the greatest potential for convective heat transfer is away from the hat surface. The suction effect is therefore an undesired effect on disc brake cooling.

Interestingly, the discussed effect of axially travelling airflow, promoted by the exiting air at the ID of the lower channels, influences the highest predicted region of h_{conv} on the brake disc; at the outboard side of the hat. The effect of the axial airflow was that it leads to a larger volume of air passing over the increased hat diameter. The characteristic length (or diameter in the case of a cylinder) has an inversely proportional relationship with heat transfer. If everything remained unchanged, a drop in h_{conv} would occur. Conversely, a peak value of 17 W/m^{2}K shows the dominance of the increased airflow volume.

5.2. Change of convective heat transfer coefficients during cooling

As previously demonstrated, most interesting changes in air flow occur around the hat region, hence the influence of lowering temperatures on convective cooling will be discussed for this region, for the end of the monitored cooling period (rotor and hat temperatures equal to 49°C). Changes in the airflow around the hat also caused changes to the h_{conv} surface dissipation patterns. Although air speeds are extremely low, approximately 0.5 m/s, Figure 16 indicates that the area of high h_{conv} values around the hat is much larger than for any other friction surface temperature. The lack of an axial momentum allows the airflow to be much more uniform across the hat rather than being pushed across to one side. The maximum h_{conv} is therefore somewhat reduced in magnitude to approximately 15 W/m^{2}K. This is still higher than on the friction surface.

The large h_{conv} area is however, a local occurrence as it is restricted to the bottom half of the hat section. On the upper half, convective HTC values are close to zero, due to insufficient airflow in this region.

With such a small volume of air flowing around from the bottom side of the hat, there is little air available to flow over the upper outboard surface.

6. Experimental investigations and comparisons with modelling results

In order to validate the CFD work, practical experiments were undertaken on the Thermal Rig. A common technique to validate CFD modelling is the hot wire anemometry method, which measures air speeds and compares them to the CFD calculated speeds, as used by many previous authors such as Galindo-Lopez [3]. In buoyant conditions, the air speeds will be a whole order of magnitude lower than in dynamic applications so it was not possible to use the hot wire anemometry validation technique. Alternatively, a method based on air temperatures rather than speeds was devised.

6.1. Rig set-up, heating and cooling processes

Numerous thermocouples were installed into the Thermal Rig and situated around the disc brake. Rubbing type thermocouples recorded the friction surface temperatures whilst 7 probe type thermocouples recorded air temperatures. The position of the probe thermocouples along with their corresponding reference names used in this report are identified by red markers in Figure 17. The air thermocouple naming convention starts with the circumferential angle the thermocouple is positioned relative to the vertical centreline datum, when looking from the outboard surface. Positive angles represent a clockwise position from the vertical centreline, whist negative values are anti-clockwise positions. The relative angle is followed by AO (standing for Air Outside) with the final value describing the thermocouple radial distance from the disc brake OD surface.

There were three different styles of K type thermocouples used: welded tip PTFE, probe and rubbing thermocouples. The welded PFTE thermocouples were placed at individual points around the brake assembly and held in place by heat resistant tape, typically used to measure caliper and pad temperatures (not shown in this paper). In Figure 18, probe thermocouples used to measure air temperatures are shown. It was concluded that this thermocouple type was most suitable for this task as the probe is sufficiently strong to support itself in a variety of positions, at substantial distance from the carrier. This

is seen as considerable advantage as the use of any additional support would present an obstacle and influence air flow. Rubbing/contact thermocouples have been explained in detail in Part 1 of the Paper. They are used for rotor surface temperature measurements.

As the Induction heating coil (IHC) was located on only the one side of the disc, to ensure an even distribution of heat, the disc was rotated at 100 rpm through the induction field during the heating phase. Thermal equilibrium was achieved by holding the disc brake friction surfaces at 400°C for 30 minutes, allowing the conduction process to heat the entire disc brake volume to a uniform temperature. After this time period, the IHC and motor were turned off to replicate the stationary disc brake cooling scenario. This heating sequence is described in Part 1 of this paper.

Numerous cooling tests were conducted, with some disc rotor and hub temperature results shown in Part 1 of the Paper. The tests were conducted with open and blocked vanes, with and without a heat insulating gasket between the disc (hat) flange and wheel carrier (see Part 1 of the Paper). In all cases, rubbing/contact thermocouples were used to measure disc rotor temperature, these together with hub temperature measurements were averaged, then used to calculate average disc temperature throughout the cooling period. Figure 19 shows cooling curves for the three conditions tested: disc without the thermal gasket and open vanes (as installed on the vehicle), disc with the thermal insulating gasket (inserted between the disc and wheel carrier) and open vanes, and disc with the thermal gasket and blocked vanes (using insulated tape at disc ID and OD). For each condition, the tests were repeated five times and Figure 19 shows averaged values. It is worth pointing out that the tests were very repeatable, with little deviations, with all temperatures falling within a $\pm 2\sigma_{sd}$ band (detailed uncertainty analysis was conducted in Part 1 of the Paper).

As expected, the fastest cooling was for the disc with open channels and no thermal insulating gasket installed, with the slowest for the disc with gasket and blocked vanes. Though the influence of the gasket (conductivity) seems small, the improvement with open vane cooling was not as high as expected. CFD has given some unique insight of the reasons, hence these graphs will be discussed later after evaluating heat transfer coefficients in various disc areas.

6.2. Calculation of the average convective heat transfer coefficient

Cooling curves can be used to compare measured data with predicted temperatures, but their true values are in providing information to calculate average heat transfer coefficients across disc surfaces. It would be difficult to try and calculate the heat transfer coefficients for specific areas, due to complex inter-relationships described earlier on. The values of convective heat transfer coefficients are low and their local variations not sufficiently high to produce any measurable temperature gradients on the disc surface or within the bulk of disc material. Disc cross sections are substantial and material (cast iron) conductivity quite high, rapidly 'evening out' most of the differences in local cooling rates. Exceptions are the differences between the two large areas, the rotor and hat, as described in Part 1 of the Paper. Nevertheless, in all cases, no matter which type of the modelling is used to predict the temperatures and/or heat transfer coefficients (analytical, CFD or FE), the predicted cooling curves can easily be compared and validated using experimental data.

The procedure used to calculate heat transfer coefficient from the cooling curve will be briefly presented here. The actual values of heat transfer coefficients will be presented later, when compared to analytically and CFD predicted values. Air flow experiments and air temperature measurements will be also presented later and compared with modelling results.

Figure 20 shows a typical disc cooling curve, which is used to calculate heat transfer coefficients. Throughout the cooling period, specific temperatures will be selected, forming a temperature range i.e. $\Delta T = T_i - T_{i+1}$, as shown in Figure 20. Considering that the coefficient of heat transfer for each of the three heat transfer modes (conduction, convection and radiation) has different relationship with temperature, the temperature difference ($T_i - T_{i+1}$) should be kept small. This, however lead to the errors due to uncertainties with temperature measurements (as described in Part 1 of the Paper). To minimise errors, it is most appropriate to eliminate or precisely define as many modes of heat transfer as possible. First and foremost, conductive losses can be practically eliminated by inserting a heat insulated gasket between the disc flange and wheel carrier (see Part 1 and Figure 19). To monitor the validity of this assumption, thermocouples were imbedded on both side of the interface and the premise

was shown to be true (for further detail see Stevens [7]). From Figure 19, it can be seen that conduction losses are relatively small as their influence on the cooling curve is very low.

As regard to radiative losses, Part 1 of the Paper described the experimental procedure used to establish the value of emissivity, which was shown to be constant at ε = 0.92. This provides sufficient input data to calculate heat transfer coefficients, based on the graph shown in Figure 20 and known disc geometrical and mass characteristics.

Typically, two methods can be used to predict convective heat transfer coefficients, both starting from equation (3), defining energy dissipation for the given time period (temperature range), and both giving practically identical results (see [2] and [3]). In this Paper, radiative heat dissipation will be calculated first. No doubt that convective and radiative modes have very different relationships with temperature (as detailed in Part 1 of the Paper), with radiative dissipation rapidly diminishing with temperature drop. Different sections of the disc will initially be at different temperatures, which also influences the results. However, with suitable calculation of average temperatures and keeping the temperature difference ($T_i - T_{i+1}$) under 10°C initially, with even lower ranges later, reliable results can be obtained. Obviously, as disc cools down, the corresponding times for achieving the said temperature change will increase. It is therefore appropriate to suitably reduce temperature range. This approach has become a common practice in calculating convective heat transfer coefficients in automotive, railway and other industries.

The procedure of calculating heat transfer coefficients from the cooling curve is independent of the disc state during cooling, i.e. weather it is stationary or rotating - either in still air or in a cross flow. Fundamentally, the calculation is based purely on the energy loss (heat dissipation) over a period of time. As already mentioned, the heat (energy) loss in a period of time is equal to the product of rotor mass, specific heat and temperature change for the time period:

$$\Delta E_d = m_d C_p \Delta T_d \qquad (3)$$

where, as per Figure 20: $\Delta T_d = T_i - T_{i+1}$

Assuming there is no conductive heat transfer from the disc into the wheel carrier, the dissipated energy is sum of radiative (E_{rad}) and convective (E_{conv}) heat (energy) losses:

$$\Delta E_d = E_{rad} + E_{conv} \tag{4}$$

Radiative heat power dissipation is defined by the well know equation:

$$Q_{rad} = \varepsilon\sigma A_{rad}\left({T_d}^4 - {T_\infty}^4\right) \tag{5}$$

This power changes substantially with the temperature drop, but for small temperature differences, of the order of 10°C or less, it can be assumed constant for that time period, hence the energy dissipated by radiation is equal to the (average) power multiplied by the time period:

$$E_{rad} = Q_{rad}\Delta t = \varepsilon\sigma A_{rad}\left({T_d}^4 - {T_\infty}^4\right)\Delta t \tag{6}$$

where: $T_d = \frac{(T_i + T_{i+1})}{2}$ and $\Delta t = t_{i+1} - t_i$

As all values and parameters are known, radiative energy loss can be calculated using Equation (6). In this particular case, disc surface emissivity used was ε = 0.92, as detailed in Part 1 of the Paper, Stefan-Boltzmann constant is σ = 5.67037 E-8 $Wm^{-2}K^{-4}$, A_{rad} = 0.34487 m^2, average ambient temperature 24.1°C, or in absolute temperature T_∞ = 297.2 K. Obviously ΔT_d and Δt can be suitably chosen throughout the cooling period.

As total energy dissipation within individual time periods ΔE_d (Equation 3) and radiative E_{rad} (Equation 6) are now known, the energy dissipated by convection can be calculated, as it follows from Equation (3):

$$E_{conv} = \Delta E_d - E_{rad} \tag{7}$$

Having similar approach to radiative energy and power relationship, convective energy is equal to the average power multiplied by the time period. Hence average convective power can be calculated from the known energy and the time period:

$$Q_{conv} = \frac{E_{conv}}{\Delta t} \tag{8}$$

On the other hand, the convective power is defined by a well-known relationship:

$$Q_{conv} = h_{conv} A_{conv} (T_d - T_\infty) \tag{9}$$

Finally, convective heat transfer coefficient can be calculated as:

$$h_{conv} = \frac{Q_{conv}}{A_{conv}(T_d - T_\infty)} \tag{10}$$

As the time period is the same as for radiative losses, so are the corresponding temperatures. For the considered disc, the total disc convective heat dissipation (wetted) area is A_{conv} = 0.65767 m^2, which when the ventilation channels are blocked, reduces to the same area as for radiative emission, i.e. A_{conv} = A_{rad} = 0.34487 m^2. Such a disc is actually a 'solid equivalent' of the considered ventilated disc as there is no heat dissipation from the channels and vanes.

Some assumptions and simplifications had to be made to apply this approach. The method is however of sufficient accuracy, in particular considering very slow disc cooling. It should be kept in mind that the relatively steep gradient at the beginning of the cooling curves shown in Figure 19, can be misleading as the time is shown in hours (with the total cooling time lasting 6 hours).

The results for the calculated convective heat transfer coefficients using equations (3) to (10) above, from the recorded disc cooling curves (Figure 19), will be presented in the next section, together with the analytical and CFD results.

7. Results Validation

Air velocities predicted using CFD and presented earlier in the paper (Figures 5 to 10), indicate very low speeds, under 2 m/s, which are practically impossible to measure without obstructing the flow and influencing the values to be measured. As quantitative measurements were not possible, considerable effort was directed towards providing qualitative experimental proofs for flow patterns predicted. Unfortunately, due to time and financial limitations, it was not possible to use particle image

velocimetry (PIV). Good results were obtained using smoke generator, typically used in wind tunnels, with long curved probe, and the experimentally generated qualitative results will be presented first.

7.1. Air flows around the cooling disc

To detect the airflow movement, neutral buoyancy smoke was introduced to the air. An ATE Smoke Generation unit was used to generate smoke and control the flow of smoke via a swan-neck probe. In order to produce proofs suitable for reproduction (printing and comparisons with CFD plots), various approaches were tried, from still photos to videos in varying lighting conditions. A laser plane was also generated to help trace the flow (see Figure 21). By using a special Ondina EL oil, it was possible to generate a neutral buoyancy smoke that was crucial for this work. As the oil passed through the probe it was inductively heated beyond its flash point to vaporise it, which for the used oil was 159°C. Consequently, the smoke exiting the probe was hotter than the ambient but cooled quickly due to it being relatively low in volume in comparison to the surrounding air. Being low in volume prevents the storage of thermal energy so it is dissipated quickly. Providing that the probe tip was sufficiently away from the disc surface when introducing the smoke, the elevated smoke temperatures had minimal effect on the flow patterns.

It was considered very important to prove a very specific flow pattern, shown in Figures 5 and 6, where the hot air exiting the ventilation channels at ID, from the lower half of the disc, prevents air intake into upper half (which flows from ID toward OD at the top of the rotor). This phenomenon was very obvious to the observer, when using smoke generator. It was however, more difficult to record and document. It was concluded that the best method was to video record under well-lit conditions, then replay the video and select still pictures that best the flow pattern investigated. This unfortunately led to relatively low resolution and low contrast pictures being generated. After numerous attempts, reasonably clear outputs were produced.

It should be pointed out that flow patterns changed during cooling resulting in the need to repeatedly reheat the disc. Other problems were related to the need to ventilate the area as the smoke generated rapidly filled the laboratory. Furthermore, the hot disc was hazardous to the personnel who were trying

to generate smoke in the right places and record images. Lastly, good images could only be taken in very still air, restricting any movement. Figure 21, shows such a still photo, clearly proving the flow phenomenon predicted using CFD. The air is exiting from the lower channels at rotor ID, and flowing over the hat. Laser generated light-plane, positioned in the mid-disc plane, can be clearly seen (laser light-plane experimental results are presented in Stevens [7]).

7.2. Air temperatures

The advantage of having large disc with high thermal capacity is in the amount of heat that can dissipate. Consequently, when heated to high temperatures, air around the disc should be heated to sufficiently high temperatures, with the temperature changes sufficiently slow to enable measurements and recoding of the values vs. time. Figure 11 displays considerable heat plume rising above the disc, with Figure 18 showing some of the thermocouples used to measure air temperatures. Figure 17 documents the exact position of the thermocouples used for measurements, with the same points in space used to predict air temperatures in CFD analyses. However, before discussing the output from the CFD modelling, the collection of experimental data made it possible to determine which turbulence model results is the most appropriate to use when modelling stationary parking applications and hence, which set of data will be presented.

7.2.1. Turbulence Model Comparison

The predicted air temperature values for the laminar and the three separate turbulence models under investigation are compared to the measured air temperatures in Table 2. Experimental temperatures shown are for the assumed stabilised disc temperature of 350°C and the percentage difference for each of the CFD turbulence models predicted temperatures (as detailed in section 2.2.5.). It is interesting to see that no turbulence model can claim superiority over the others for all thermocouple positions. For example, at thermocouple +000 AO 010mm the SST model produced the closest match to the measured data with only a 4.1% overestimation, as well as being best matched at two other locations, whereas it was considerably poorer than the laminar prediction at position +045 AO 010mm. Little differentiation is seen from the results for the air temperatures on the lower half of the disc. Generally, the SST results

approximately differ by 10% to the measured data in absolute terms, and less than 20% in when temperatures are converted into relative terms. With good agreement between the SST model and the measured data, the CFD modelling can be described as accurate even with the reduced heat transfer CFD convergence level.

Although the differences of around 10% might be considered large, it is worth pointing out that CFD still offers unique insight into the cooling process, unable to match by any other modelling or experimental techniques. The predictions are extremely valuable in all aspects, air flow patterns, air flow velocities, air temperatures and heat transfer coefficients.

The SST turbulence model was also one of the fastest, only slightly slower than Laminar. Both of the commonly used turbulence models, the BSL model and the $k-\varepsilon$ model, took longest to run (see Table 1) but offered little in terms of advantage in accuracy. The lack of kinetic energy in the air flow around the brake disc prevented these models from generated the accuracy that has often been associated to them in the braking industry for rotating disc. It can be concluded from this investigation that the SST turbulence model was the most appropriate when simulating natural convection around a disc, for both accuracy and computational time advantages. However, it should be noted that the laminar model results produced quite satisfactory results too.

By using equation (11) an estimate of the Re value can calculated at 2.2×10^4, taking air property values at 100°C and assuming a velocity of 1 m/s. According to Allen [9], this value falls within the unsteady laminar region, where the flow is transitioning from laminar to turbulent. This prediction matches well with the analytical modelling in Part 1 of this paper. A laminar or early stage transitional period over the disc brake friction surfaces is detrimental to brake cooling as the additional turbulent energy helps to increase flow velocity, which in turn increases the amount of convection. It can be concluded that of the four models used, it is the SST model that is the most appropriate to use in stationary applications to ensure the low energy inflow turbulence is captured.

$$Re = \frac{\rho v L}{\mu} \tag{11}$$

Table 2: CFD results compared to experimental results, % difference from measured.

Thermocouple	Measured Temperature K	CFD model Laminar Δ%	$k-\varepsilon$ Δ%	BSL Δ%	SST Δ%
+000 AO 010mm	528	9.2	-9.8	8.4	4.1
+000 AO 215mm	391	-13.7	-18.5	-13.8	-12.3
+000 AO 395mm	340	-4.1	-8.7	-5.2	-3.8
+045 AO 010mm	322	1.9	-3.7	7.4	7.1
+090 AO 010mm	327	-10.3	-10.5	-10.3	-10.3
+135 AO 010mm	324	-9.6	-9.6	-9.6	-9.7
+180 AO 010mm	326	-10.2	-10.1	-10.1	-10.2

7.2.2. Heat Plume Validation

The above comparisons are conducted at the mid-plane of the disc. It is interesting to compare predicted and measured temperatures in the axial direction from this plane. A distinct velocity plume is clearly generated directly above the disc, which does not extend to the extremities of the disc brake width. As the air is accelerated around the hat section, gaining heat as it does so, a plume of this nature would be expected. Nonetheless, four further thermocouples were positioned on the Thermal Rig, located in accordance with Figure 22, to test the validity of CFD results.

Results are displayed in Table 3. Once again, CFD predictions matched well to the measured data, showing the existence of the predicted plume. Air temperature remained at ambient for three of the four additional thermocouple locations with only the outboard side temperature rising by a marginal amount,

which was not captured by the CFD simulation. This result was attributed to the fact that only the disc was in the model, whereas in reality the wheel carrier was also attached forming a larger assembly, increasing the length of heat source in that direction. Table 3 also shows good correlation with the measured temperature values, using the SST turbulent model again and setting the ambient temperature at 20°C. Despite some differences, CFD predictions follow the trends measured and provide unique insight into the air temperatures. It should be noted that experimental values are very sensitive to any air movement in the laboratory.

Table 3: Plume test results

Thermocouple Position	Temperature [°C]	
	Measured	Measured-CFD
+000 AO 395mm	67	-13
+000 AO 395mm +22.5mm Outboard	28	- 8
+000 AO 395mm +22.5mm Inboard	21	+ 4
+000 AO 395mm +22.5mm Vanes Left	20	+ 1
+000 AO 395mm +22.5mm Vanes Right	20	+ 1

7.3. Convective heat transfer coefficients

Finally, to complete this analysis, the predicted average values of h_{conv} produced by the CFD simulations for the inboard, outboard, hat and vane surfaces are presented in Figure 23, for the corresponding rotor temperatures of 350°C, 213°C, 112°C and 49°C (the corresponding hat temperatures are 200°C, 175°C, 112°C and 49°C respectively). In the same figure, analytically calculated heat transfer coefficients (derived in Part 1 of the paper) are presented in the line form, for the entire temperature range. Predictions of the rotor values (inboard, outboard and vanes) are coloured in red whilst hat predictions are green.

7.3.1 CFD results

CFD values will be discussed first, with all analyses conducted for a ventilated disc (the channels were not blocked), with values available for all local areas, as well as averaged across specific areas or the entire disc. To begin, Figure 23 shows the h_{conv} values averaged across each friction face (inboard and outboard), vanes (channels) and hat areas.

It can be seen in that there is little difference between h_{conv} values on the inboard and outboard friction surfaces at the beginning of the cooling, when the disc was heated to 350°C, as there is inboard friction surface shows only a slightly lower value. Decreasing the friction surface temperature to 213°C sees the outboard surface value of h_{conv} reduce at a faster rate than the inboard, the tendency which remains throughout the cooling. The reason for such behaviour is related to the flow around the hat. It has already been shown that as the temperature reduces, the axial velocity component of the air flowing around the hat diminishes, pushing the localised outboard stagnation point towards the OD (see also Figures 5, 8 and 13). Below the stagnation point, there is a volume of low energy air, which isn't joining the free-stream flow, causing an area of low heat convective dissipation. Hence, as the stagnation point increases in height, the area of low dissipation increases and ultimately reduces the total outboard surface h_{conv}. Overall, for the entire considered temperature range (from 350°C to 49°C, for the ambient temperature of 20°C) there is a drop in average h_{conv} from 12.5 to 8.7 W/m^{2}K for the outboard, and from 12.0 to 10.2 W/m^{2}K, for the inboard rotor friction surface.

Looking at the vane h_{conv} values (within cooling channels), a decrease in h_{conv} was predicted using CFD between the temperatures of 350°C and 213°C, as would be expected (Figure 23). However, when looking at the next temperatures range, from 213°C to 112°C, a slight increase was predicted. This can be attributed to the phenomenon already discussed in relation to the flows shown in Figures 5, 6, 8 and 14. Ejected air from the lower vane channels, at the ID, flows around the hat section and prevents the air entering at higher temperatures (Figure 5), whereas the situation changes with temperature decrease and more air can get into the upper channels (Figure 8). Consequently, for the entire considered

temperature range (from 350°C to 49°C) there is only a slight drop in average h_{conv} in the channel areas, from 7.4 to 6.2 W/m^{2}K, for the ambient temperature of 20°C.

On the hat surface, in general, CFD predicts drop in average h_{conv}, from 6.2 to 3.9 W/m^{2}K, for the temperatures shown, of 350°C, 213°C, 112°C and 49°C (Figure 23). However, it should be taken into the consideration that the actual hat temperatures are lower when the disc is hot, and the corresponding hat temperatures are 200°C, 175°C, 112°C and 49°C respectively. As demonstrated in Part 1 of the Paper, there are some fundamental differences in convective heat transfer from disc surfaces (vertical wall) and hat (cylinder). Despite h_{conv} values for the hat area being relatively close to those of the vanes, it should be emphasised that vane (channel) wetted area is over three times larger. Combined with typically higher temperatures, the total contribution of vanes ('ventilation system') is much higher than for the hat, which is even more emphasised in the moving vehicle.

7.3.2. Analytical results

Analytical h_{conv} values produced in Part 1 of the Paper are also shown in Figure 23, allowing a direct comparison to be made with CFD results. It should be noted that analytical modelling neglected channels and vanes, practically assuming a solid disc, or even more precisely just a solid thin wall. Unfortunately, it was not possible to repeat CFD modelling for this condition. In a qualitative sense, analytically predicted values match well with the CFD predictions, demonstrating a similar form, with regards to the decrease in value with temperature reduction. CFD results plateau at higher temperatures slightly more than the analytical results, suggesting less h_{conv} variation with temperature. There are however further differences. Analytical predictions are lower for the disc (rotor) friction surfaces than corresponding CFD results but higher for the hat.

7.3.3 Average experimental, analytical and CFD h_{conv} values for the entire brake disc

From the measured temperatures on disc surfaces, as per the cooling curves shown in Figure 19, average convective heat transfer coefficients were extracted and presented in Figure 24. The procedure used is described in Figure 20 and associated equations (3) to (10). For both cases presented in Figure 24 a

thermal insulating gasket was installed between the disc and wheel carrier to minimise conductive heat losses. The procedure explained earlier on (equations (3) to (10)) clearly shows that radiative heat losses will be unaffected by blocking the channels. However, looking at the temperature curves shown in Figure 19, temperature differences between the blocked and open channels are relatively small. It is interesting to see the effects on average convective heat transfer coefficients h_{conv} for these two cases. As described before, accurate prediction of local heat transfer coefficients from experimental measurements is not possible (due to low heat dissipation rates, high disc mass, high material conductance etc.).

Figure 24 shows average convective heat transfer coefficients h_{conv} calculated from measured cooling curves (Figure 19) for the ventilated disc with open channels ('Ventilated Disc – Experimental') and blocked channels ('Solid Disc- Experimental'), together with CFD and analytical predictions. Clearly, measured values are at the extremes of values shown, at least for temperatures above 80°C. The highest h_{conv} have been measured for the solid disc (i.e. blocked vanes). This might come as a surprise but looking at the CFD predicted values at Figure 23, and cooling curves in Figure 19, this makes perfect sense. Cumulative wetted area of the vanes and channel (see Paper 1, Figure 2 and Table 2) of approx. 0.313 m^2 is almost identical to the wetted area of the disc friction surfaces and hat area (approx. 0.345m^2), i.e. the wetted area of the disc with blocked channels (i.e. the solid disc). Convective heat transfer coefficients in channels (vanes) are much lower (Figure 23), whereas the rate of cooling (Figure 19) is not much slower.

Figure 24 also shows average convective heat transfer coefficients predicted using CFD. As the CFD analyses were conducted only for the ventilated disc (without blocking the channels, 'Ventilated Disc – CFD'), that curve was actually predicted. However, for comparison purposes, using the values from Figure 23, the average heat transfer coefficient for the entire 'solid disc', excluding channels, was calculated, and for the temperature range presented in Figure 24 as Solid Disc 'Equivalent' – CFD. Although such a methodology is not strictly correct, due to the flow through the channels affecting the flow (hence heat transfer) over the friction surfaces (as showing in sections 4 and 5), it gives an

opportunity for interesting comparisons, obviously with due caution. It is clear that this CFD curve follows quite closely the experimental h_{conv} curve. At the beginning, at 350°C, experimental values are about 20% higher but the differences reduce with the disc cooling down, with the CFD and measured values being equal at about 85°C. At lower temperatures CFD over predicts cooling rates.

Analytical results shown in Figure 23 were also used to calculate equivalent solid disc cooling, with the values averaged proportionally to the size of the corresponding areas. The resultant curve 'Solid Disc – Analytical', is very close to the CFD for the solid disc, lower by only about 5% throughout the entire temperature range. Analytical approach could not include influence of the vanes nor the relative influence of the rotor (considered as a solid vertical wall) and hat (considered a cylinder). Therefore, physically, this was closer to the measured values for the disc with blocked vanes. The analytical method under predicts h_{conv} compared to the experimental values, in particular at higher temperatures but the nature of the curve is the same and the discrepancy diminishes during cooling. At 250°C, measured values are about 20% higher, at 100°C about 10% and the values become identical at 50°C for the ambient temperature of 20°C. Although these differences might be considered high, analytical method is very simple to apply and results corrections can be introduced in practical applications.

Finally, for the ventilated disc 'as is', the CFD predictions are very close to the experimental h_{conv} values. Over predictions are of the order of only 5% at the beginning at 350°C, but slightly increasing during the cooling. At 100°C the difference is just over 20%. The calculated values are extremely useful and proving that reliable calculations for solving practical engineering problems are possible.

8. Discussions

The most interesting finding for the anti-coning disc design considered was that relatively fast moving air exiting the lower vane channels at the disc ID, travelling axially, creates a blockage to the upper channel inlets. With the lack of air entering the upper channels, heat transfer capabilities are vastly reduced. Air flow restriction was found so severe in one particular case that a dual-recirculation was predicted within a single vane-channel, stifling all the flow through the entire channel.

Predicted airflow patterns were backed up by the smoke machine testing, coupled with the light plane; the use of this technique was novel within the braking sector. A lack of smoke detected on the upper channel exit light plane proved the inability of the disc brake geometry to funnel airflow through these channels. Combining the smoke machine testing with the CFD flow simulations lead to the conclusion that the CV anti-coning, straight vane disc brake design does not cool optimally during a parking application. Consequences of this are that the disc brake remains at a higher temperature for an extended period of time, transferring surplus amounts of heat energy into the caliper. Elevated caliper temperatures can expose thermally sensitive components, located within the housing, to higher temperatures.

CFD simulations also produced predictions of surface h_{conv} distribution. Inboard and outboard friction surfaces distributions were both relatively constant, at approximately 11 W/m^{2}K, at high surface temperatures. In channel values were just under half of those predicted at the friction surfaces.

The complex three-dimensional flow predicted from the CFD ensured a difference between the two sets of values would be present, yet there were limitations in the simulation process preventing the result from matching better numerically. The areas of extreme h_{conv} values consistently located towards the edges of the model. It was said originally that these areas will have little impact on the predicted airflow predictions because of their relatively low surface area. This still holds true for the predicted airflow patterns, as proved in the smoke machine validation process. However, calculations of the mean h_{conv} will be drastically hampered by the recorded edge errors as these localised values, in excess of 120 W/m^{2}K, increased the total surface average somewhat beyond the analytical values. Again, the only feasible way to remove this error from the simulation process would be to increase the mesh density at the geometry edges. This was not done due to the computational power and time constraints associated with making these changes.

CFD is no doubt a very powerful tool or achieving this task, having much progressed from the early day's application presented by Daudi [10]. It is interesting to consider any improvements that a brake designer can do in order to generate new rotors with more effective convective cooling in stationary

conditions. As mentioned in Part one of the Paper there is very little published work on stationary discs, as the vast majority of papers deal with rotating discs. Still, some of the approaches and results can be used as experience and inspiration in improving disc static cooling. The approaches described by Voller et al. [11], Angelinas [8], McPhee and Johnson [12], Galindo-Lopez and Tirović [13] and Liang et al. [14], give some intersting, helpful ideas. Furthermore, Zhang [15], Repmann [16], Stephens et al. [17], Zamitt [18], Barigozzi and Perdichizzi [19] all offer some insight into improving cooling of the roating discs.

However, the concept of a straight or curved vane optimised for pumping is not compatible with the demands for improving static disc cooling, when flow blockages need to be avoided. An old idea, partly abondonded in CVs nowadays was to use pillred ventilated rotor designs, in order to improve cooling in stationary conditions, mostly for city busses. With the improvements in casting processes and rotor thermo-mechanical structural optimisation, this type of discs certainly offers advanteges. It is difficult to quantify gains in convective cooling at this stage but the work published by Wallis et al. [20] and Palmer et al. [21] certanly help in directing the ideas and overall research. It should be poited out here that much wider use of pillar type discs in high performance passanger cars is driven by the need to improve Noise Vibration and Harshness (NVH) characteristics, at the account of sacrifising some of the air pumping and related deterioration of convective cooling at higher speeds. No doubt that such designs offer advantages in static cooling too. Overall, the problem of improving static cooling seems to be more challenging than for the rotating disc. Obviously, both operating conditions are to be taken into consideration when finalising the design.

9. Conclusions

Part 2 of this Paper focused on the generation of an accurate temperature prediction methodology using the CFD tool, for a stationary brake disc. As very little work of this nature had been previously conducted, there was little advice in the literature as to how to setup the model. Stationary braking airflows were proven to have a complexity level of at least dynamic braking application, if not more complex. The demand for a finer mesh and modelling of the entire disc, without the possibility of

introducing periodic boundary conditions, considerably increased running times but gave unique insight into the physical processes modelled. The flow patterns change with temperature drop, which is hardly detectable in a rotating disc, particularly at higher angular velocities.

An air temperature based validation method was devised that numerically assessed the results of the CFD simulations by comparing them to measured data, achieved through the cooling test procedure. CFD proved to be a very powerful tool in predicting brake disc cooling performance. However, the modelling requires attention to detail, large number of cells, powerful computers and long CPU times. SST and Laminar turbulence models showed to give results closest to the experimental values and also run twice as fast as k-ε and BSL models.

The most interesting finding was the flow pattern, not previously known for this disc type. At high temperatures, deflection of the air streams happens in two forms, the first being the influence of the outer disc brake surfaces. Accelerating air below the disc brake rises vertically and is forced to deflect when it comes into contact with the relatively bluff circumferential surface. Considerably more air is deflected around the outside of the disc brake than what enters the lower vanes (90° to 180°). Air exiting from these lower vanes, at the ID, accumulates some axial momentum in addition to the vertical momentum, due to the disc brake geometry, becoming the second source of airflow deflection. Exiting airflow subsequently travels over the hat section, producing the fastest predicted air speeds of anywhere in the domain, with values reaching 1.7 m/s. This flow stream prevents fresh air intake into the upper channels, reducing disc cooling characteristics. At lower disc temperatures this effect gradually disappears, and consequently the coefficient of convective heat transfer (h_{conv}) within the disc ventilation system (vanes and channels) reduces very little with temperature drop, even showing some initial increase. In contrast, and as expected, h_{conv} on disc friction surfaces and hat section reduces with temperature drop. As presented, the maximum average surface h_{conv} is predicted for the outboard rotor friction area, equalling 12.5 W/m^{2}K at 350°C, with the lowest h_{conv} value being 3.9 W/m^{2}K for the hat area at 49°C.

Finally, the Thermal Rig proved to be of extreme importance in conducting brake thermal research. In addition to validating CFD and analytical models in terms of air patterns flows, air temperatures and h_{conv} values, it enables accurate formulation of the conductive and radiative heat losses, which are not possible theoretically to predict. Validations have been direct and indirect. For instance, as air velocities are very low, under 2 m/s, hence practically impossible to measure, smoke tests proved very useful in visualising and confirming air flow patterns predicted using CFD. Most importantly, the Rig enabled measurement of cooling curves and, from them, calculation of average convective heat transfer coefficients.

Comparisons of experimentally derived heat transfer coefficients with analytical and CFD values proved the validity of all the models and approaches developed. This was true for the entire temperature range, i.e. disc cooling from 350° to 50°C. CFD predictions for the ventilated disc were within 5 to 10% of the experimental values, typically over predicting the cooling rate. Analytical method enabled good predictions for the solid disc (i.e. disc with blocked channels), typically under predicting the convective heat transfer coefficient for higher temperatures and under predicting for lower (under 85°C). Still, considering the difference is only 10% at 200°C, analytical approach can be considered reliable and is very quick and easy to implement. As such both CFD and analytical methods are powerful design tools with own advantages and some limitations.

It is proven beyond any doubt, theoretically and experimentally, that the average convective heat transfer coefficient for the solid disc is higher than for the equivalent ventilated design in stationary conditions. No doubt the ventilated disc cools faster but for exploiting the full benefit, large wetted area of the 'ventilation system' (i.e. vanes and channels) is needed. Furthermore, the design must ensure good flow through the channels and must not imping air flow over the friction faces.

CFD remains a very powerful tool in understanding current discs and their geometrical characteristics, pointing out to the advantages and problems caused by the fundamental concept and various features. This enables generation of new designs with improved cooling characteristics. The consideration of the

pillared ventilation system, instead of straight (uninterrupted) vane seems to offer potentials worth investigating. In addition, the experience shows that such designs typically also offer NVH advantages.

Predicted and measured h_{conv} values are of utmost importance for further work, which is addressing cooling of the entire brake assembly, which in addition to the disc, contains the pads and caliper. Such a complex assembly, having the total mass of nearly 100 kg, and heated to temperatures in excess of 400°C, presents a further challenge in predicting temperatures of individual parts throughout the long cooling period, lasting several hours. As explained in Part 1 of the Paper, the motivation for this research is the introduction of Electric Parking Brake (EPB) in commercial vehicles. In hot parking conditions, when parking on a gradient, there is real danger of vehicle rolling away as the disc and pads cool down and shrink, with the caliper heating up and expanding. Presentation of the complex heat paths and changes in flows and temperatures, including their effect on braking efficiency, are the subject of the next Paper by the authors.

The research is important for two principle reasons; for the commercial vehicle EPB development, where more complex models and instrumentation can be used, and for establishing a simplified, yet robust and accurate on-board thermal model, for temperature predictions and EPB control (clamp force, re-clamping etc.) on actual, production vehicles. The work presented in Part 1 and Part 2 of this Paper presents an important step in achieving these goals.

Acknowledgement

The authors would like to acknowledge and thank Meritor HVBS (UK) and Engineering and Physical Sciences Research Council (EPSRC) for co-sponsoring the research project though EngD scheme. Special thanks to Jonathan Jackson, Dr Ralf Leiter, Paul Roberts, Martin Taylor and Peter Gibbens at the Meritor Cwmbran facility.

References

1. Olphe-Galliard M. Study of the Thermodynamics and Fluid Mechanics Involved in the Cooling of Brake Discs. MSc Thesis, Cranfield University, UK, 2011.

2. Voller GP. Analysis of Heat Dissipation From Railway and Automotive Friction Brakes. PhD Thesis, Brunel University, UK, 2003.

3. Galindo-Lopez CH. Optimisation of Convective Heat Dissipation from Ventilated Brake Discs. PhD Thesis, Cranfield University, UK, 2008.

4. Fluent Inc. Release Notes for FLUENT 6.3, 2006.

5. Jerhamre A and Bergstrom C. Numerical Study of Brake Disc Cooling Accounting for Both Aerodynamic Drag Force and Cooling Efficiency. SAE Paper 2001-01-0948, 2001.

6. Menter FR, Lamgtry R and Volker S. Transition modelling for general purpose CFD codes. In: *6th International Symposium on Engineering Turbulence Modelling and Measurements*, Dordrecht, Netherlands, 2006, pp.277-303.

7. Stevens K. An Investigation into Heat Dissipation from a Stationary Commercial Vehicle Disc Brake in Parked Conditions. EngD Thesis, Cranfield University, UK, 2013.

8. Angelinas S. Design Strategies for the Thermo-Mechanical Optimisation of Heavy Duty Brake Discs. PhD Thesis, Cranfield University, UK, 2013.

9. Allen JE. *Aerodynamics The Science of air in motion,* Second Edition, HarperCollins,1982.

10. Daudi AR. 72 Curved Finsand Air Director Idea Increse Airflow through Brake Rotors, SAE Paper 1999-01-0140, 1999.

11. Voller GP, Tirović M, Morris R et al. Analysis of automotive disc brake cooling characteristics. *Proc IMechE Part D: Journal of Automobile Engineering,* vol. 217, no. D7, 2003, 657-666.

12. McPhee AD and Johnson DA. Experimental heat transfer and flow analysis of a vented brake rotor, *International Journal of Thermal Sciences*, vol. 47 (4) 2008, 458-467.

13. Galindo-Lopez CH and Tirović M. Understanding and improving the convective cooling of brake discs with radial vanes. *Proc IMechE Part D: Journal of Automobile Engineering,* vol. 22, no. D7, 2008, 1211-1229.

14. Liang L, Jian S and Xuele Q. Study on Vehicle Braking Transient Thermal Field Based on Fast Finite Method Simulation. SAE paper 2005-01-3945, 2005.

15. Zhang JJ. A High Aerodynamic Performance Brake Rotor Design Method for Improved Brake Cooling, SAE paper 973016, 1997.

16. Repmann C. Investigation of the Thermal Behaviour of Vented Disc Brakes by means of CFD. In Breuer B. editor, *Advanced Brake Technology*, pp. 51-75, SAE International, 2003.

17. Stephens A, Watkins S and Dixon C. Aerodynamic Testing of a Vented Disc Brake. SAE paper 2003-01-0932, 2003

18. Zamitt JP. Ventilated Disc Designs – Optimisation of Heat Dissipation. MSc Thesis, Cranfield University, UK, 2007.

19. Barigozzi A and Perdichizzi A. Combined Experimental and CFD Investigation of Brake Discs Aero-thermal Performances, SAE paper 2008-01-2550, 2008.

20. Wallis L, Leonardi E, Milton B et al. Air flow and Heat Transfer in Ventilated Disc Brake with Diamond and Tear-Drop Pillars. *Numerical Heat Transfer, Part A: Applications: An international Journal of Computation and Methodology,* 41(6-7), 2002, 643-655.

21. Palmer E, Fieldhouse J and Mishra R. Optimisation of Pin Shape and its Configuration for a Pin Type Vented Brake Disc using CFD. In: *FISITA 2006 World Autmotive Congress*, 22-29 October 2006, Yokohama, Japan.

List of Figures

Figure 23: Area specific convective heat transfer coefficient: CFD and Analytical

Figure 24: Average convective heat transfer coefficients: Experimental, Analytical and CFD

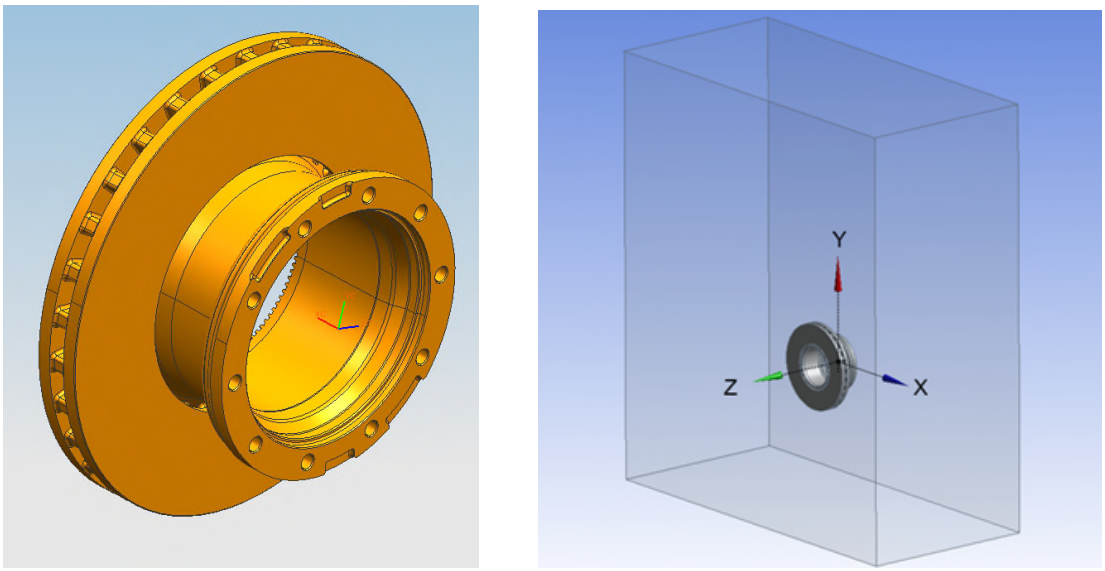

a) **b)**

Figure 1: Brake disc: a) 3D CAD solid model; b) CFD model domain analysed

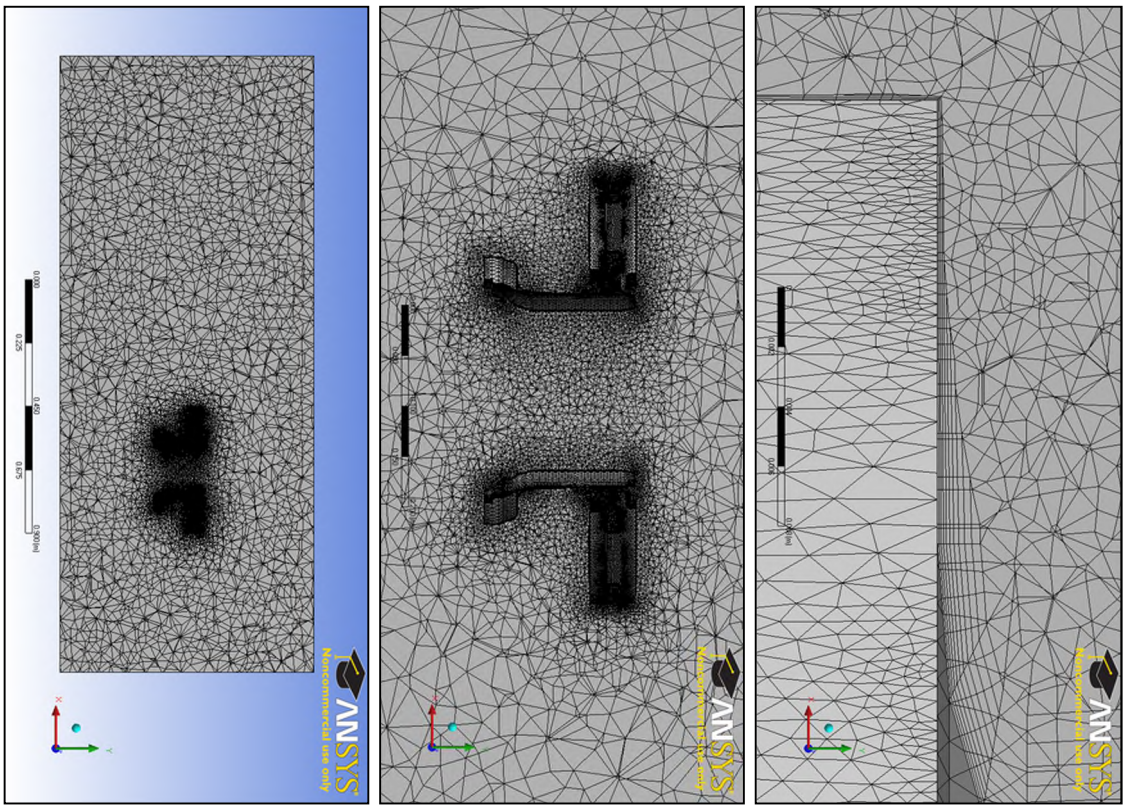

a) **b)** **c)**

Figure 2: Mesh generated for CFD investigation: a) The full volume mesh; b) Finer mesh around the disc; c) Prism layer in surface proximity

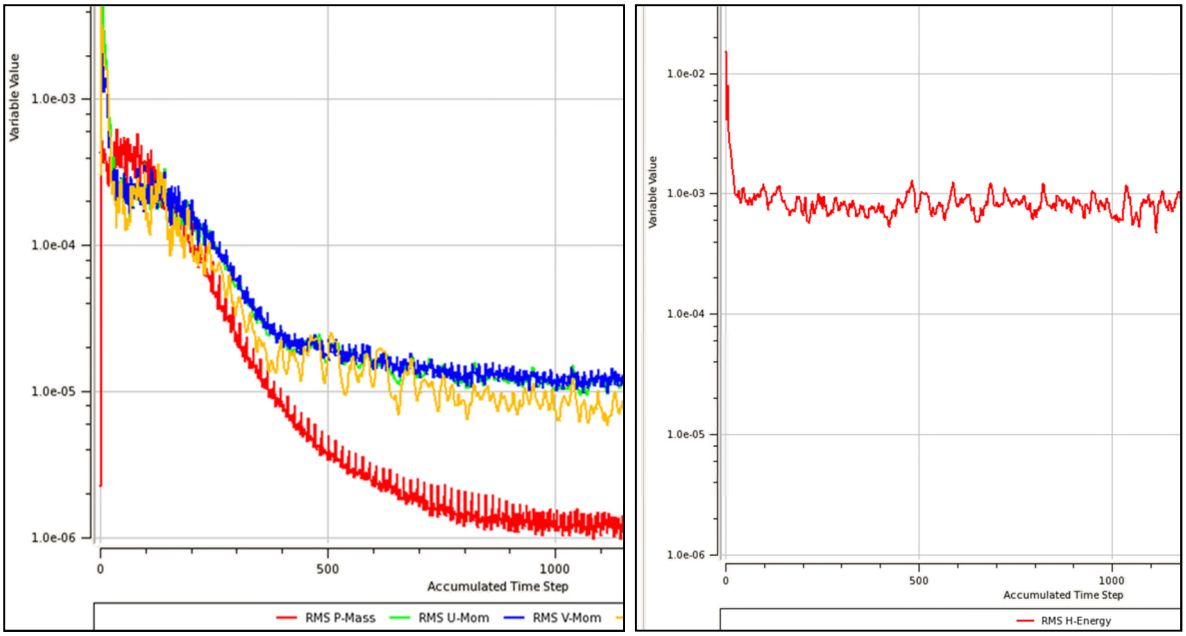

a) **b)**

Figure 3: Typical convergence graphs for: a) Mass and momentum; b) Heat transfer

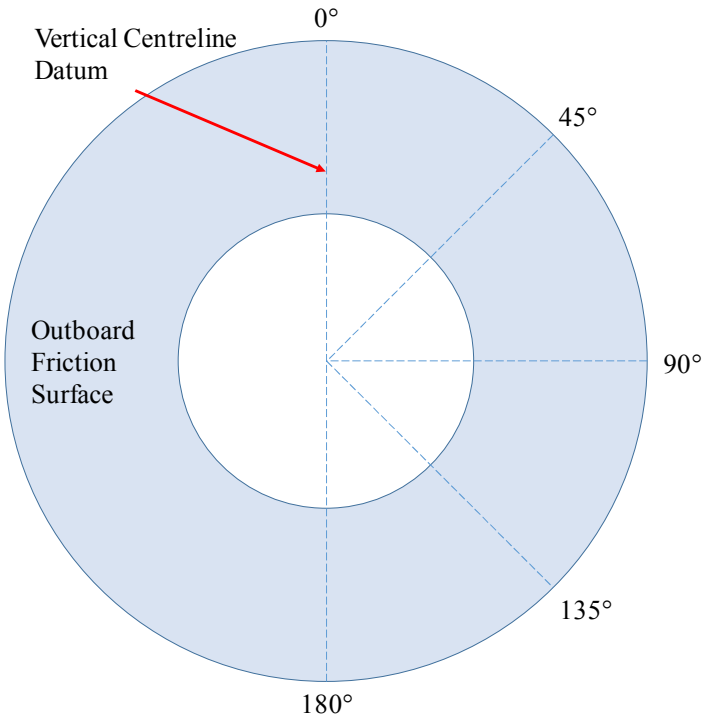

Figure 4: Relative positions of the flow channels from around the brake disc

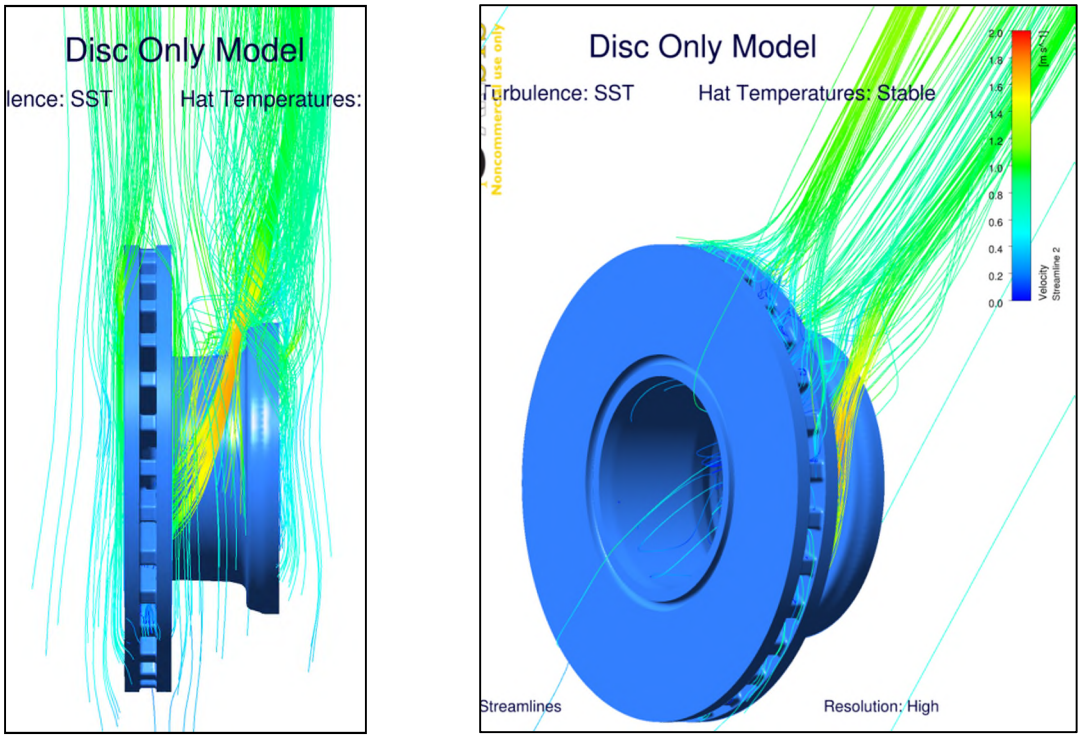

Figure 5: Velocity streamlines from the vanes mid-plane for rotor at 350°C

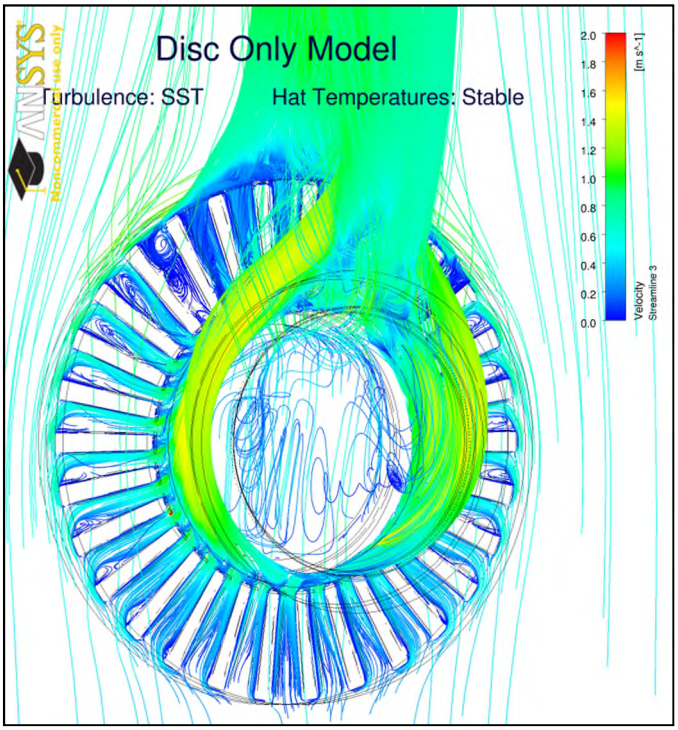

Figure 6: Velocity streamlines within the vane channels at 350°C (surfaces have been removed)

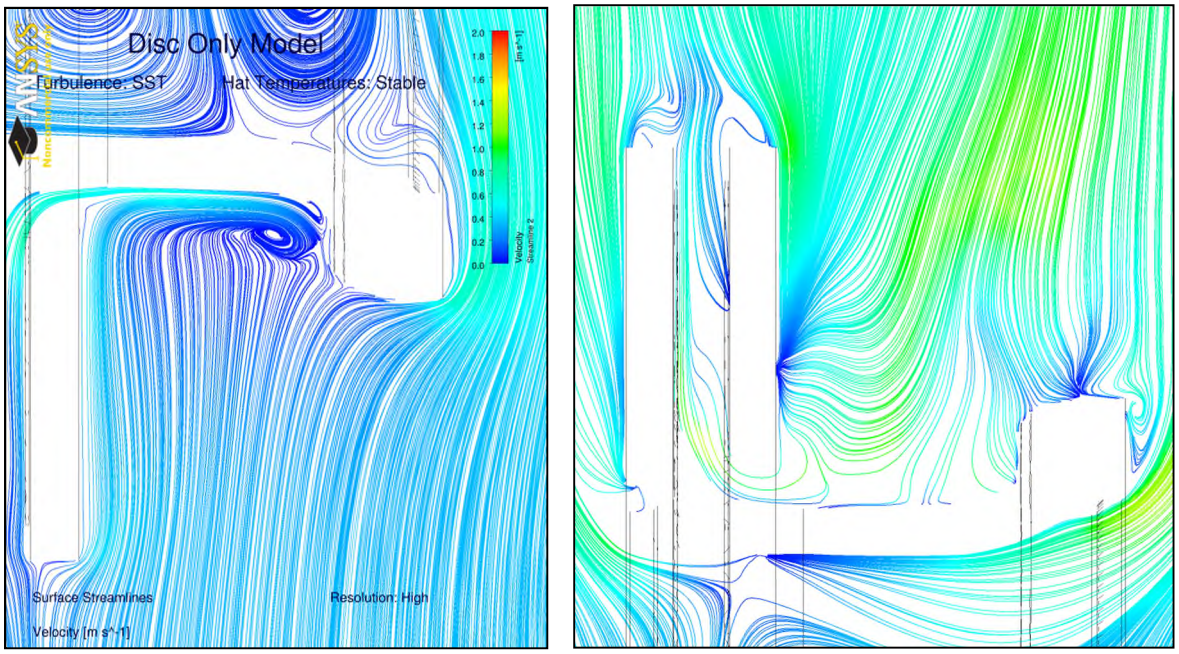

a) **b)**

Figure 7: Hat velocity streamlines at 200°C: a) Lower part; b) Upper part

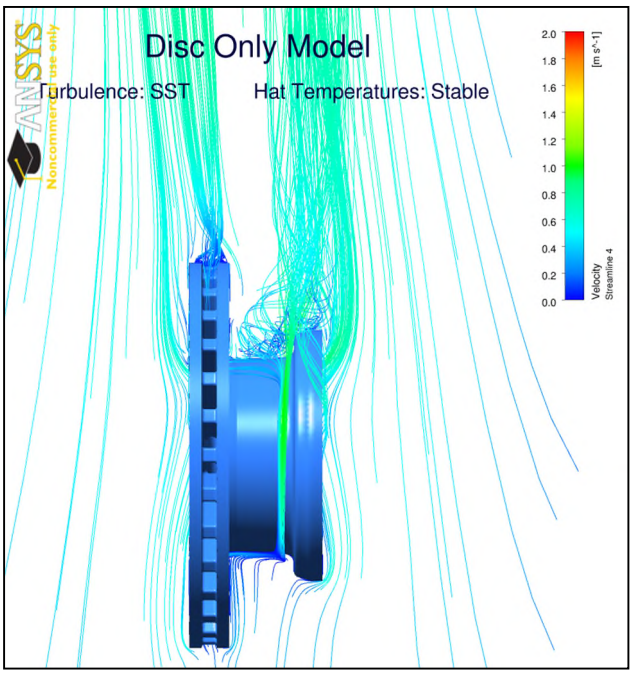

Figure 8: Velocity streamlines from the vanes mid-plane for rotor at 112°C

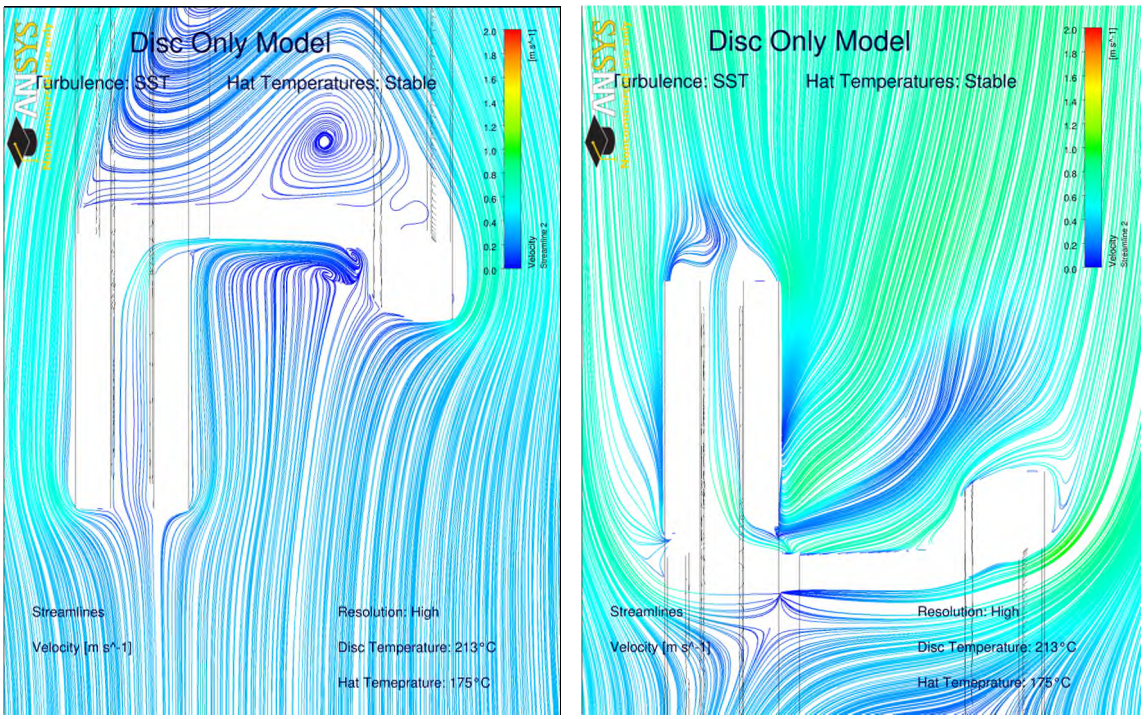

a) **b)**

Figure 9: Hat velocity streamlines at 175°C: a) Lower part; b) Upper part

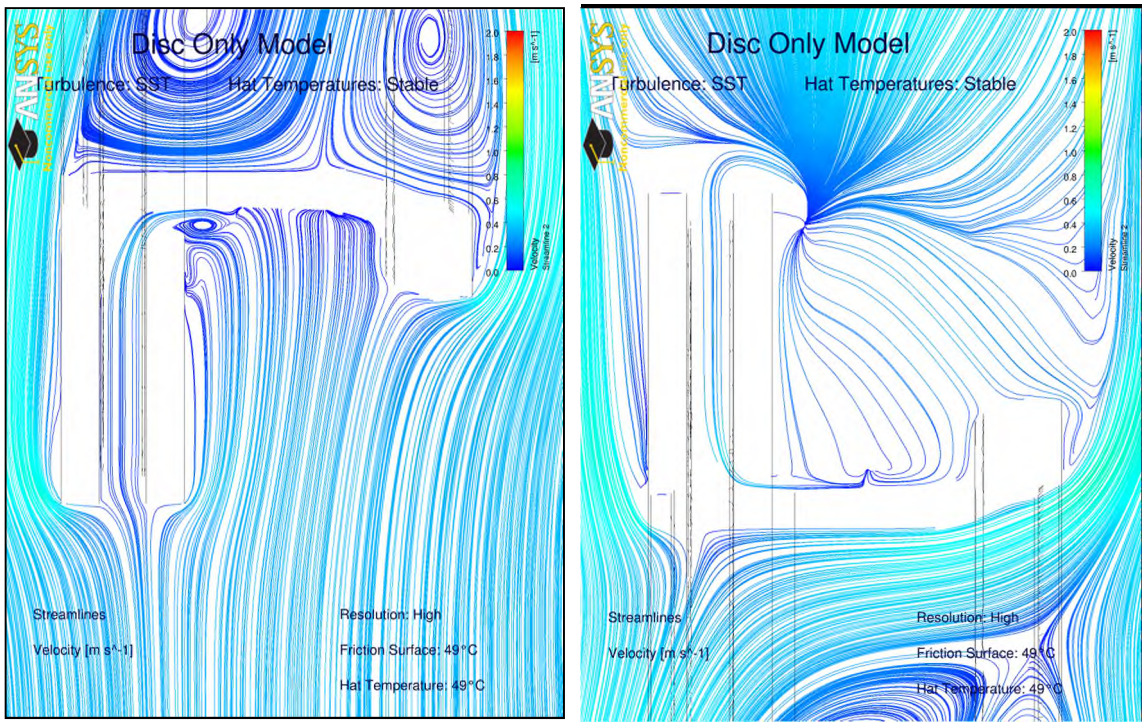

a) **b)**

Figure 10: Hat velocity streamlines at 49°C: a) Lower part; b) Upper part

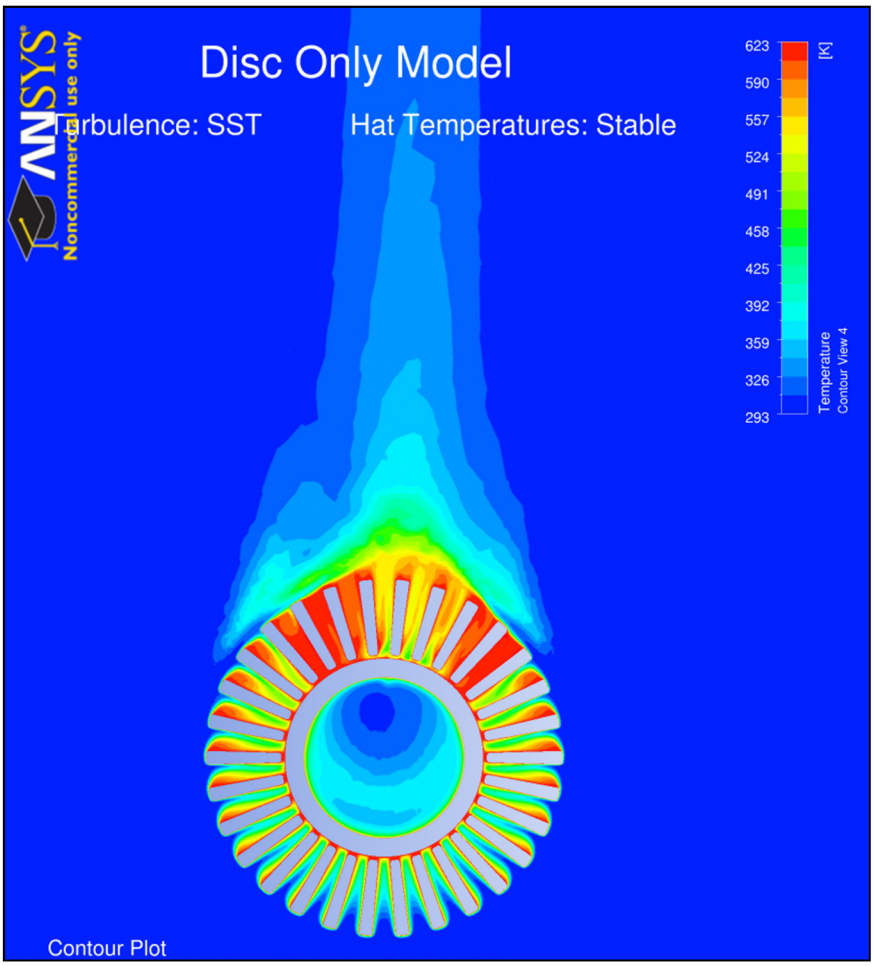

Figure 11: Air temperature distribution in the mid-plane of the disc, for rotor at 350°C

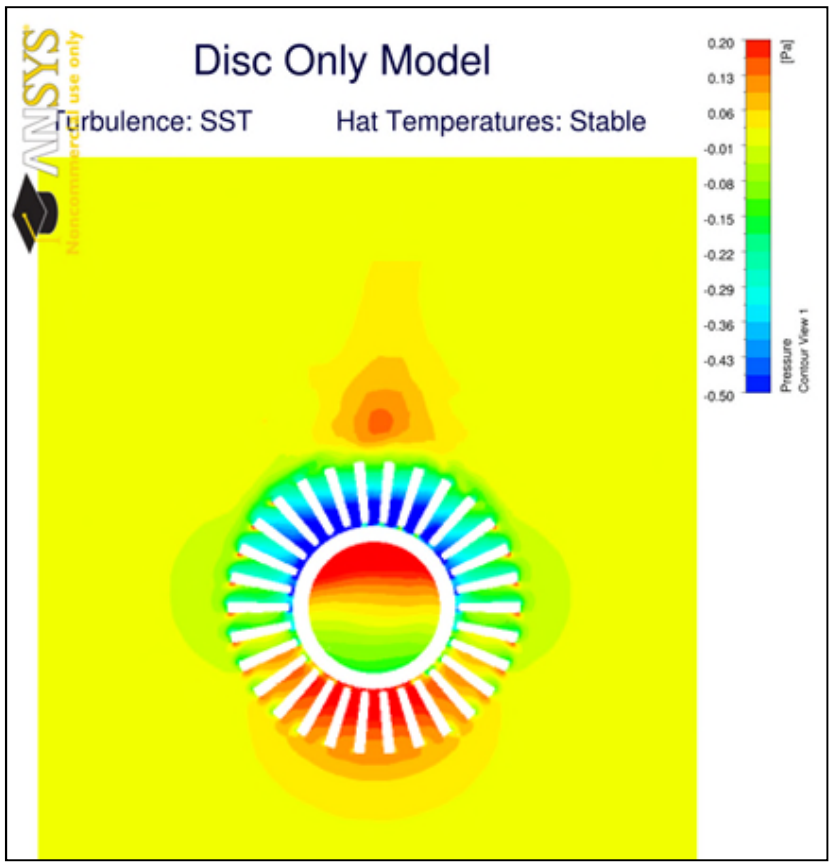

Figure 12: Air pressure change from atmospheric (rotor at 350°C)

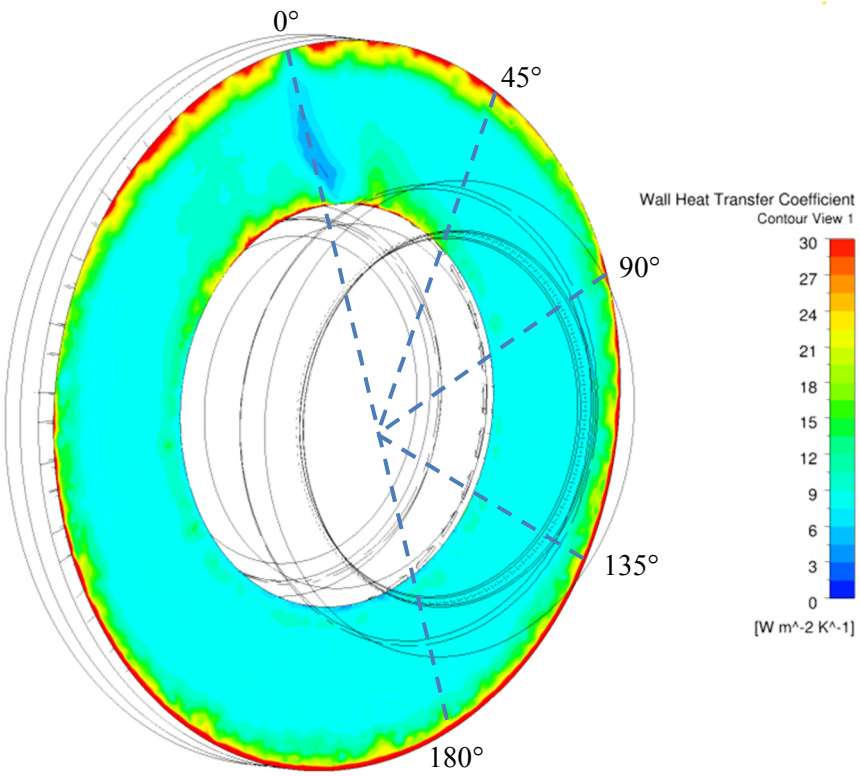

Figure 13: h_{conv} distribution off the outboard rotor at 350°C

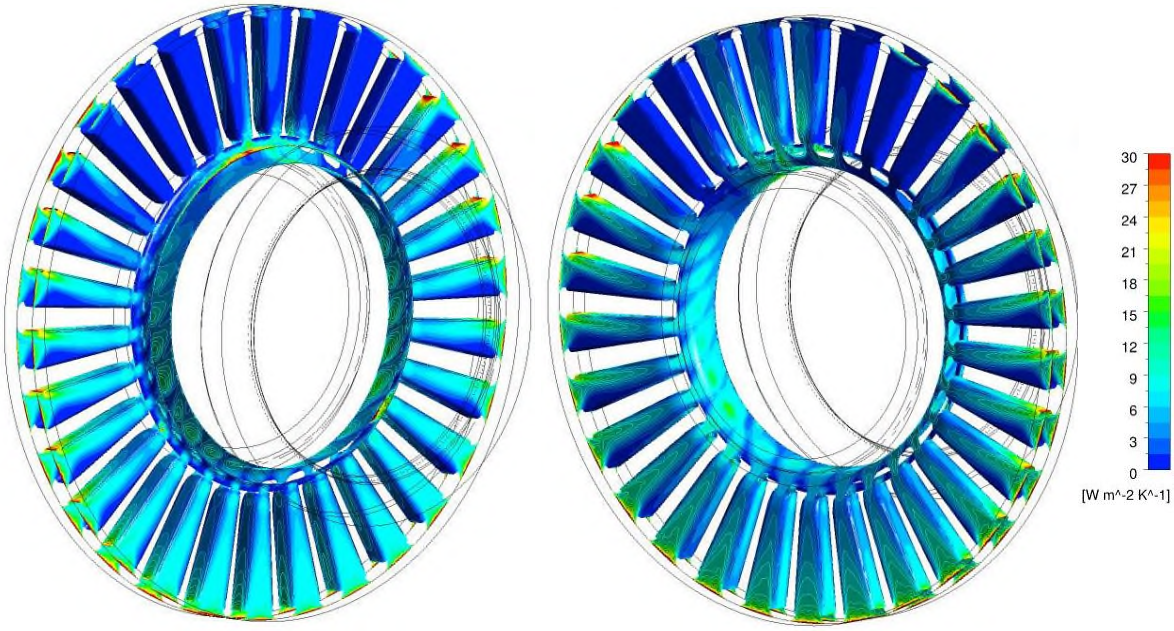

Figure 14: h_{conv} distribution in the ventilation channels for rotor at 350°C

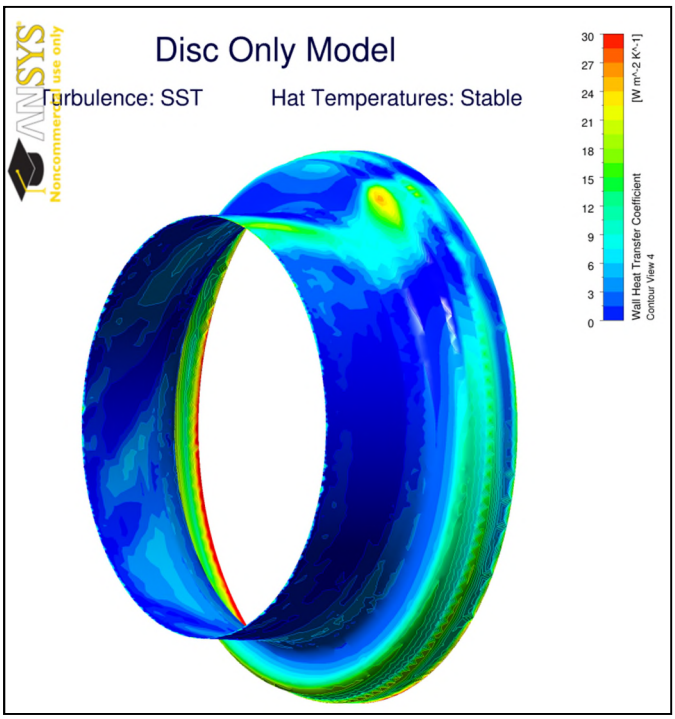

Figure 15: Convective heat transfer distribution over hat section outer surface (hat at 200°C)

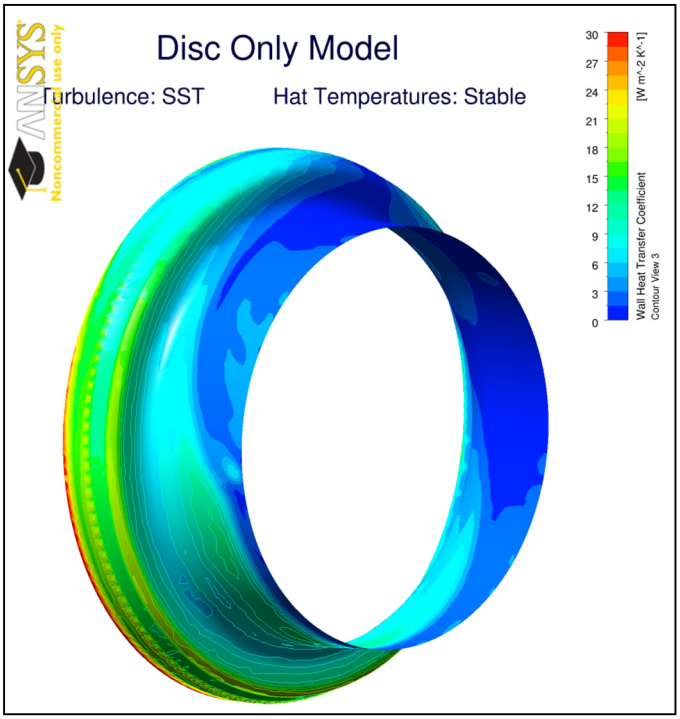

Figure 16: Convective heat transfer distribution over hat section outer surface (hat at 49°C)

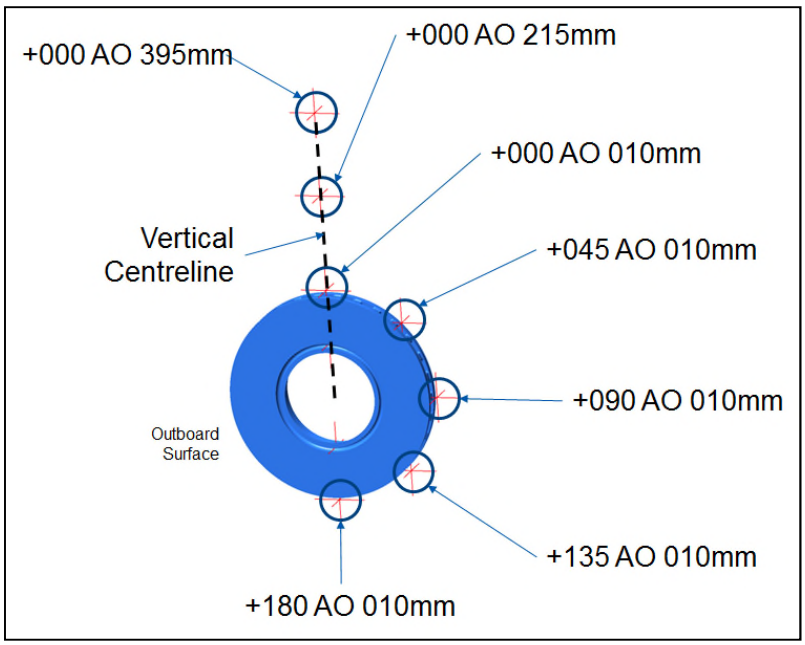

Figure 17: Thermocouple names and positions.

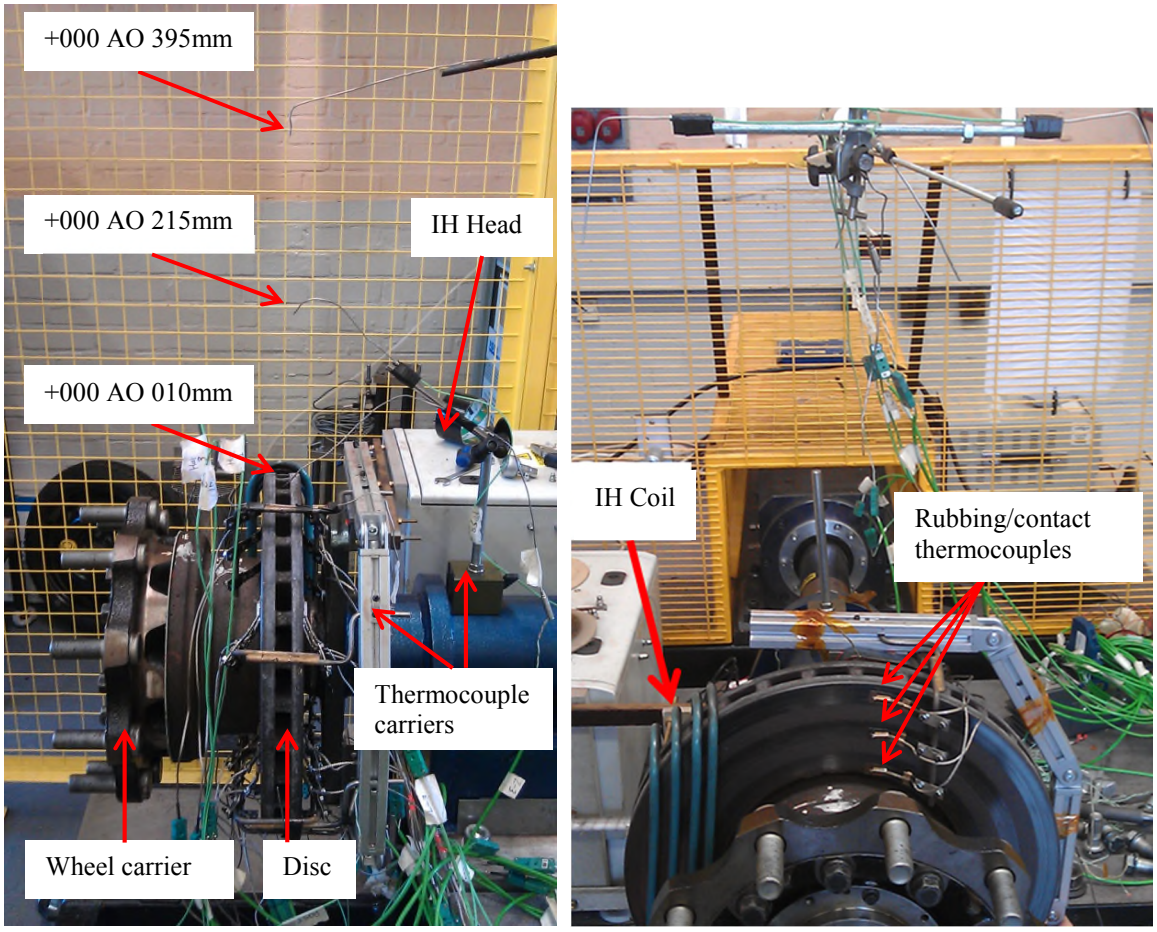

a) **b)**

Figure 18: Brake disc installed on the Thermal Rig: a) probe thermocouple positions; b) Front view showing Induction Heating Coil and rubbing/contact thermocouples

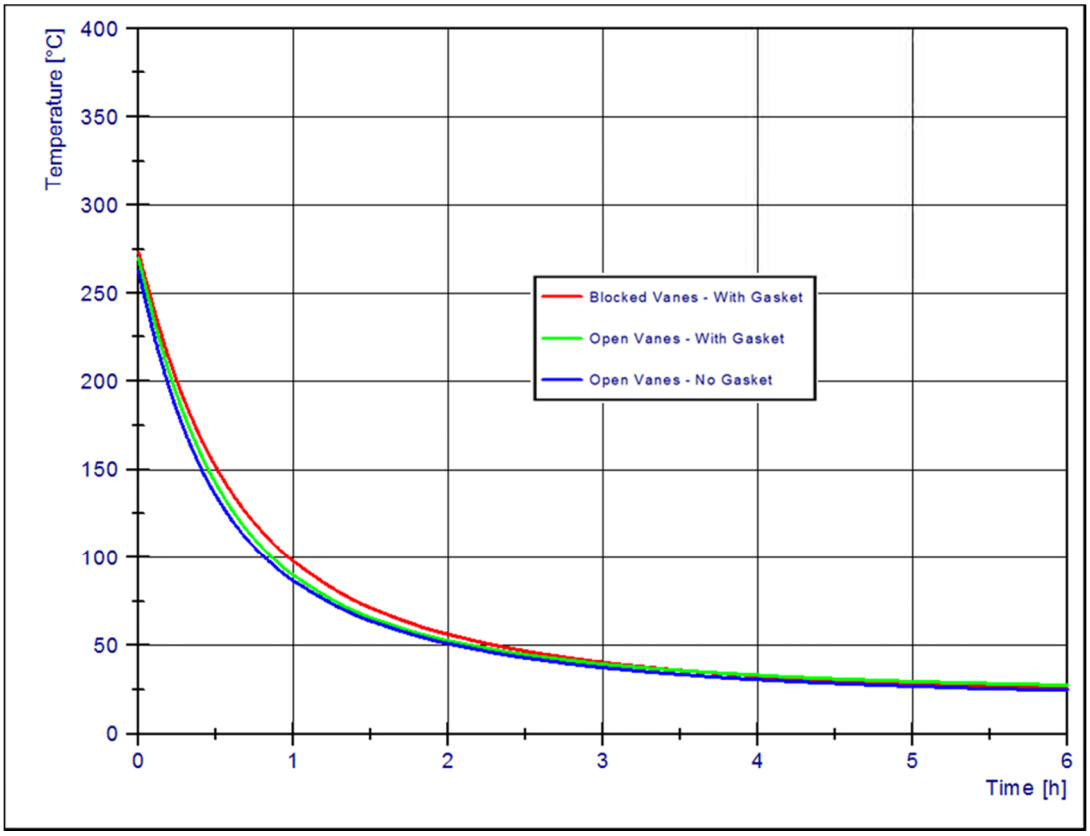

Figure 19: Average disc temperature during cooling for the three conditions tested

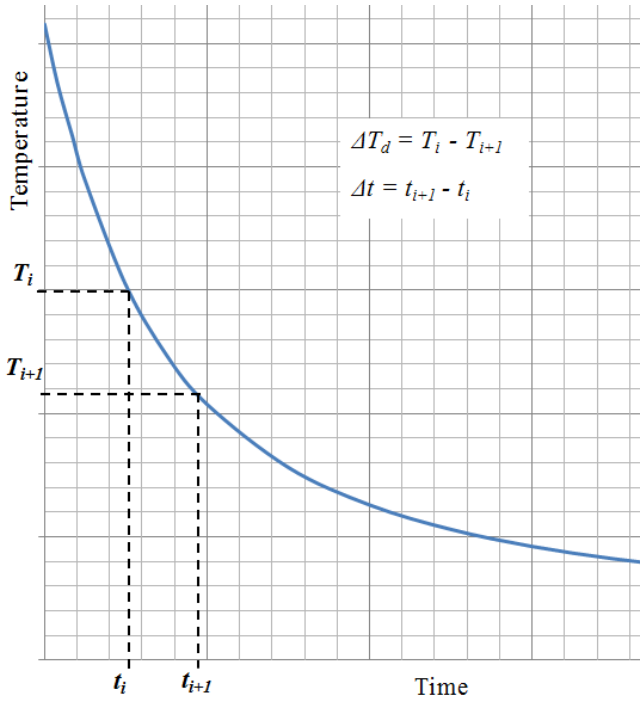

Figure 20: Typical disc cooling curve

Figure 21: Smoke tests - evidence of exiting ID airflow causing the upper inlet blockage (laser red light marking rotor mid-plane)

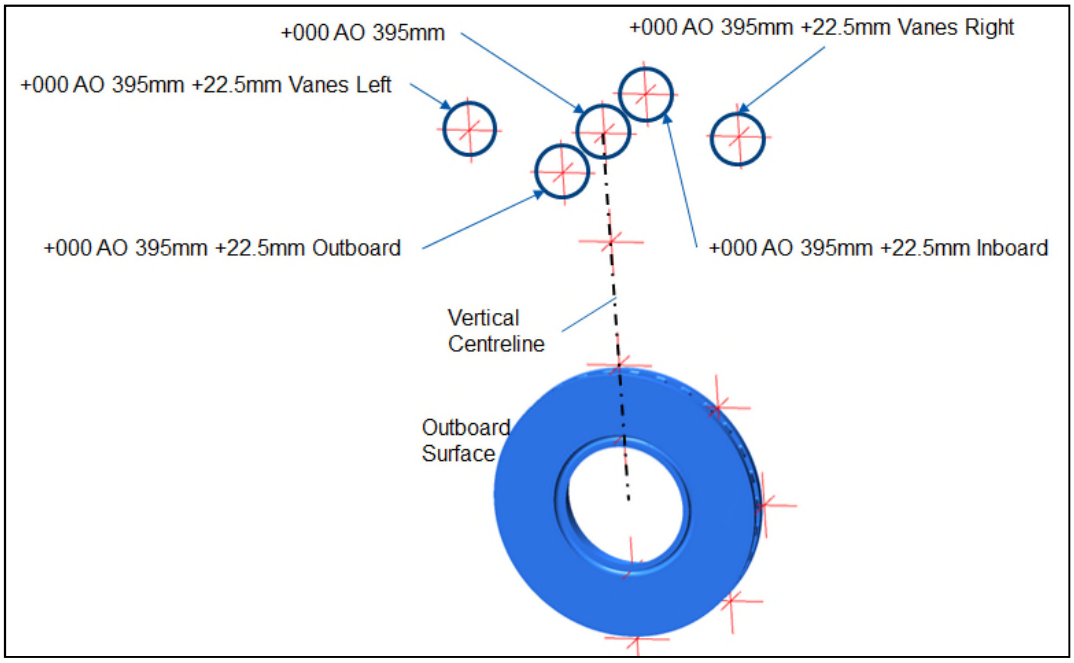

Figure 22: Additional thermocouple positions for plume existence test

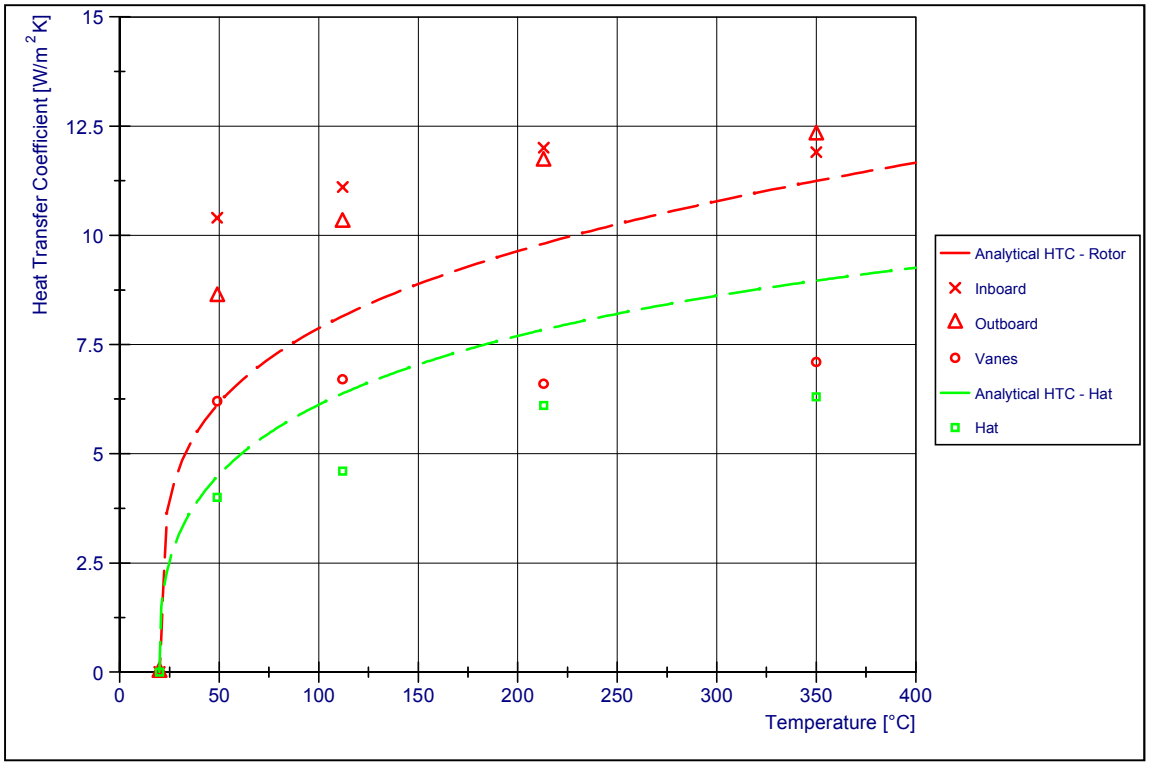

Figure 23: Area specific convective heat transfer coefficient: CFD and Analytical

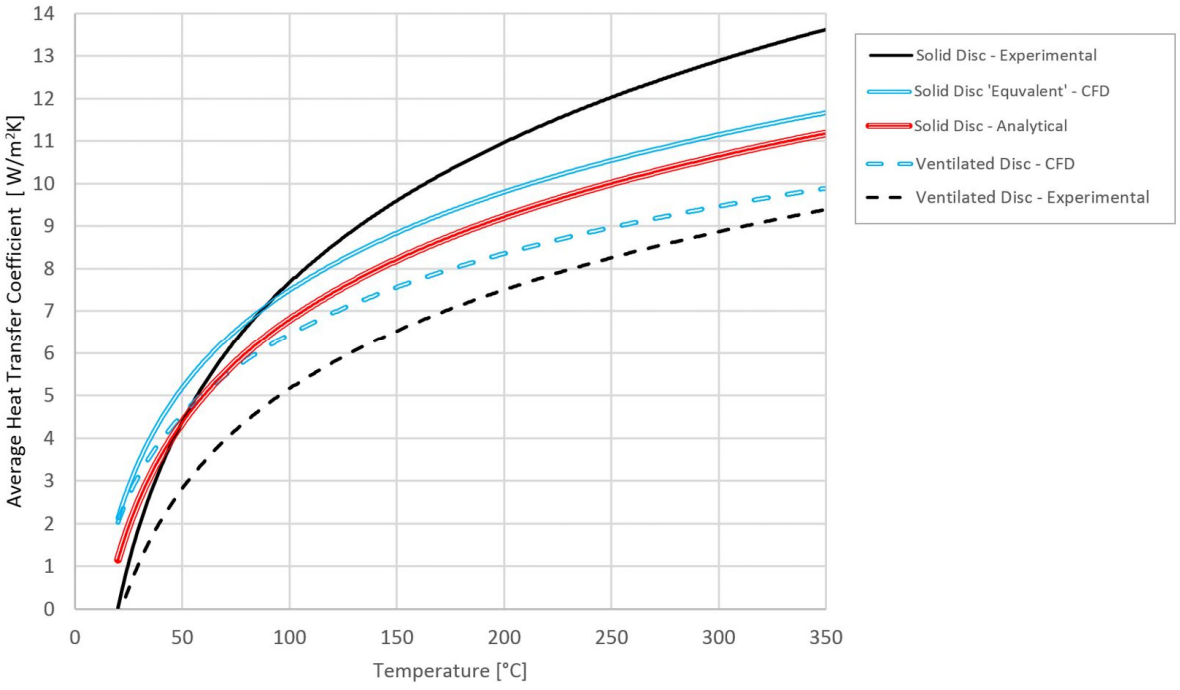

Figure 24: Average convective heat transfer coefficients: Experimental, Analytical and CFD

2017-05-18

Heat dissipation from a stationary brake disc, Part 2: CFD modelling and experimental validations

Tirovic, Marko

SAGE

Marko Tirovic and Kevin Stevens. Heat dissipation from a stationary brake disc, Part 2: CFD modelling and experimental validations. Proceedings of the Institution of Mechanical Engineers, Part C: Journal of Mechanical Engineering Science, Vol. 232, Issue 10, 2018, pp. 1898-1924
http://dx.doi.org/10.1177/0954406217707984